UNIVERSITY OF CALIFORNIA
RIVERSIDE

Atomistic Studies of Structure-Property Relationships of Defects in Amorphous and Crystalline Solids

A Dissertation submitted in partial satisfaction
of the requirements for the degree of

Doctor of Philosophy

in

Materials Science and Engineering

by

Tina Mirzaei

Spring 2022

Dissertation Committee:

Dr. Peter Alexander Greaney, Chairperson
Dr. Reza Abbaschian
Dr. Sinisa Coh

The Dissertation of Tina Mirzaei is approved:

Committee Chairperson

University of California, Riverside

Acknowledgments

I owe a debt of gratitude to my advisor, colleagues, classmates, friends and family; all of whom have played a tremendous role in terms of guidance, research and life in general. I cannot thank you all enough for the impact you have impressed upon me.

Foremost, I would like to express my deep and sincere gratitude to my research advisor, Professor P. Alex Greaney, for his unconditional support and guidance throughout my research. I will always be grateful for your willingness and patience to teach and explain concepts, and also for your contribution towards my personal development.

To my colleagues, whose inspirational discussions improved the quality of my research. To my supportive friends, for their care and encouragement along this journey. To my beloved parents and brother, for their continuous love and emotional support. Without you none of these academic achievements would have come to fruition. To my fiancé, for all the passion and love he devoted to me. I am forever grateful for your encouragement and endless support throughout this adventure. I dedicate this dissertation to them.

ABSTRACT OF THE DISSERTATION

Atomistic Studies of Structure-Property Relationships of Defects in Amorphous and Crystalline Solids

by

Tina Mirzaei

Doctor of Philosophy, Graduate Program in Materials Science and Engineering
University of California, Riverside, Spring 2022
Dr. Peter Alexander Greaney, Chairperson

Amorphous materials have a wide variety of applications and their mechanical, optical, electronic and magnetic properties hold great promise towards current technologies. Just like in crystalline materials, the bulk properties of amorphous materials are often dictated by defects and other structural anomalies or outliers. However, unlike crystalline structures, amorphous materials lack long range order and the disordered nature of their atomic arrangements poses major challenges toward building a quantitative correlation between their local atomic environments, leading to complications in characterizing the structure and relaxation in these materials. This dissertation is composed of three separate studies that together build a methodology for describing and understanding the role of defects in amorphous materials. In one of the projects, the structures of the defects are all well-defined but their mechanical response is unknown and is the focus of our study. On the other hand, the other two studies involve understanding the structure of non-crystalline materials. In one of the studies, the challenge is in characterizing the average structure, its relationship to viscosity, characterizing thermodynamically-driven changes in structures, and quantifying the degree of amorphousness. In a final study, we identify the outliers in amorphous materials, we use metrics of structure and then we find the corresponding mechanical behaviour and response of these outliers. These three combined can establish relationship between defects, defects' structure and their properties in materials. In this thesis, firstly, we investigate the phenomenon of fragility in amorphous liquids, which characterizes the dynamics of amorphous glass-liquid and refers to the sensitivity of liquid's bonding network and is associated with non-Arrhenius dependence of the liquid's viscosity. We demonstrate how fragility in amorphous liquids correlates with atomic size-mismatch which is an important consideration in the design and structural performance of glass forming alloys. Secondly, new computational methods are put forward to explain the numerical values of some useful amorphous configurations to achieve a greater understanding of the relationship between their processing, structure, and properties. Understanding the structure and the weaknesses of amorphous materials is of great importance to determine their physical and mechanical properties and to improve the materials' design. For this purpose, predictive models were developed to accurately classify and identify the defects in amorphous materials and characterize their structural features. We also illustrate the effect of different cooling rates on these local weaknesses. Lastly, we studied the evolution of the thermal conductivity in pristine $LiAlO_2$ and we elucidated the effects of defects on its thermal properties at different scales which is important to assure its long-term performance and to address these defects appropriately. These contributions are anticipated to enhance our understanding of structure-property relationships of defects in materials, leading to establish useful approaches in searching for materials with desirable performance.

Contents

List of Figures

List of Tables

Chapter 1

Introduction

The goal of this thesis is to understand and explore the defects' structure of amorphous and crystalline materials and to establish structure-property relationships in these systems. Despite the abundance of amorphous materials and their usage, it may come as a surprise that there is a little known about the defects in their structures. Understanding the structure of amorphous materials plays a key role in improving the performance in their future applications. Amorphous structures' crucial distinction from a crystal involves their lack of long-range order. Amorphous structures have disordered nature of atomic arrangements and the atoms in these materials adopt varying local atomic packing configurations and may have potential defects to various degrees [1, 2]. We have shown the amorphous and crystalline structure of Cu in figure 1.1 for comparison.

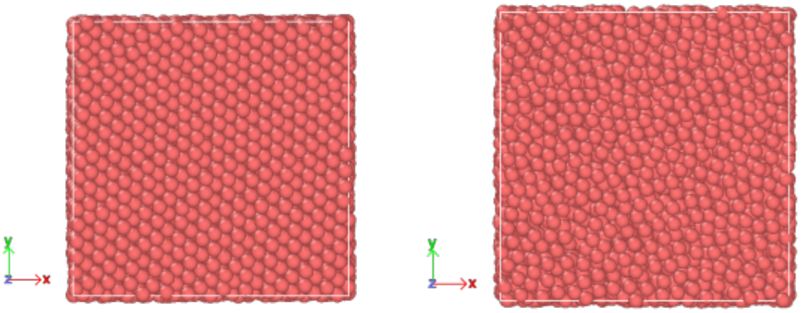

(a) (b)

Figure 1.1: Systems of (a) crystalline and (b) amorphous Cu.

In general, various classifications of solids fall into the amorphous category, ranging from amorphous polymers and ceramics to random alloys and metallic glasses; and the local outliers may act as the material's weakness in any of these categories and they may limit their applications. In this study, we characterize the defects in materials by identifying variations in packing behaviour of materials, providing structural characterization, and involving the use of novel computational methods and structural metrics to evaluate and compare their properties.

As a starting point for this thesis, we present how the defects in crystalline structures are different from the ones in amorphous structures and we also present a high level picture of some of the universal features of amorphous solids along with a brief description of the amorphous materials that we are specifically focusing on (this is covered in the remainder of the first chapter). In chapter 2, we elaborate on the novel computational methods that we employed followed by the details of the characterization metrics in chapter 3. Chapter 4 enhances our understanding of the nature of the thermodynamically-driven changes in amorphous structures and characterizing the dynamics of glass-liquids. In chapter 5, we present our results on identifying the outliers in amorphous materials and quantifying the mechanical behaviour and the response of these local outliers. Chapter 6 mainly focuses on the defects in crystalline structures which are all well-defined and we present our findings on the evolution of the thermal conductivity in pristine crystalline $LiAlO_2$ as well as the defective $LiAlO_2$. In the last chapter of this thesis, we conclude the study by summarising the key research findings in relation to the structure-properties relationships of materials and discussing the value and contribution thereof. We will also review the limitations of this study and propose avenues for future research in amorphous materials.

1.1 Defects in Crystalline vs. Amorphous Materials

In crystalline solids, defects are defined as any imperfection and deviation from the perfect arrangement of atoms [3]. Figure 1.2 shows some of these defects in crystalline structures. Different types of defects [4, 5] in crystalline structures include:

- Intrinsic point defects [6] such as vacancies and interstitials;
- Chemical impurities such as substitutional or interstitial atoms;
- Extended defects such as dislocations, stacking faults, grain boundaries [7, 8].

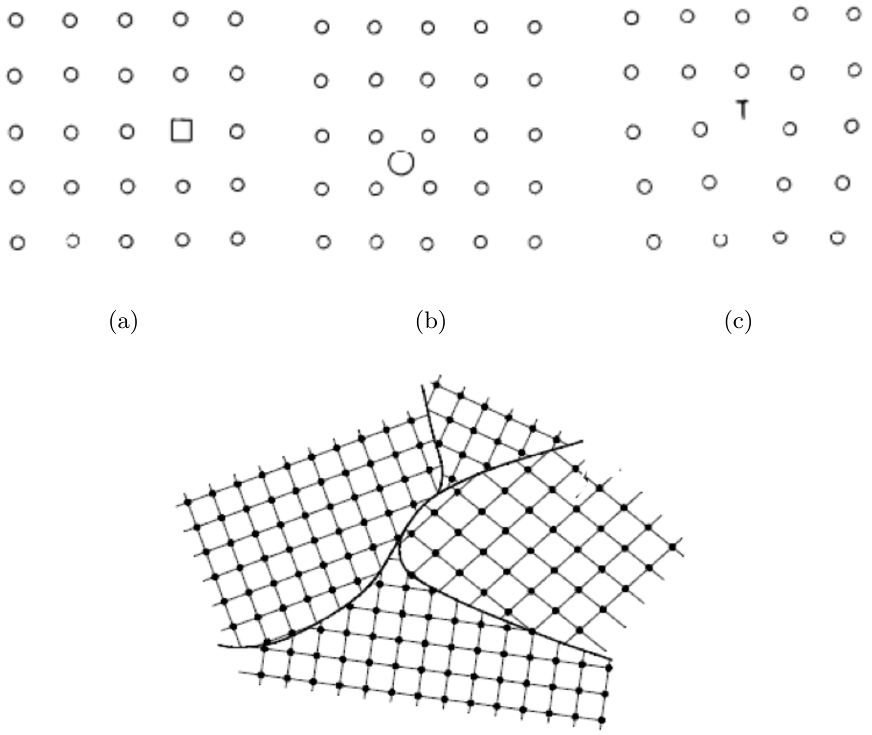

(a) (b) (c)

(d)

Figure 1.2: Example of defects in crystalline structures, (a) vacancy: when an atom is missing from one of the lattice sites (b) interstitial: when an atom occupies a normally unoccupied site in the crystal structure (c) dislocation: line along which the whole rows of atoms in a crystal are arranged anomalously (d) grain boundary: a planar defect that occurs where two crystallites meet.

However, amorphous materials lack long-range order of atoms, leading to complications in defining the defects. The main challenges in identifying the outliers in amorphous systems are: i) is there any ideal reference structure to be compared with the amorphous structure for defining the defects? ii) can defects be described as counterparts to the well-defined defects in crystals? iii) how big should the size of the region of the identified defects in the amorphous materials be? We try to answer these questions and outline the results in the next chapters.

1.2 Bulk Metallic Glasses

Among the amorphous materials, bulk metallic glasses (BMGs) [9] have a wide range of use and they have stimulated widespread research enthusiasm due to the fact that amorphous BMGs possess unique properties including high strength, high corrosion resistance [10] and high fracture toughness [11]. These promising properties have allowed them to be utilized in several technological applications such as in biomedical science [12], aerospace, as plastic-replacement components in cosmetic applications (e.g., watches, cell phones) and in structural applications (e.g., golf clubs, hardware for defense) due to their energy absorbing structures. These materials have the ability to precisely net-shape into the complex geometries and they have stable chemistry [13] which enables them to have potential applications in fabrication of complex implants and devices. The most important feature of BMGs that, along with other glasses, distinguishes them from general amorphous materials is the glass transition, where the super-cooled liquid turns into a glassy state when cooled rapidly from high to low temperature [14]. The cooling rate is a critical parameter that determines if the alloy can transform into a glassy state, such that the liquid can be quenched at a sufficiently high cooling rate to suppress the formation of equilibrium crystalline phases [15]. Fast cooling prevents regular crystallization, and thus the material keeps the structure of the precursor liquid. The cooling rate is typically found to be in the order of 10^5–$10^6 Ks^{-1}$ for glass formation [16].

While a vast number of traditional and non-traditional methods have been used to analyze these amorphous materials, there is still little known about their structures. Current knowledge of short-range order is insufficient to determine the overall structure of a disordered glass and the effect of defects on their properties.

Our research on metallic glasses is closely related to that on metallic liquids in supercooled area. We specifically study the structure of the common bulk metallic glasses: Zr-based family metallic glass (such as AMZ4) [17] and Pt-based family metallic glass (such as Pt42, Pt60). We cover more details of their structures and properties in chapter 4 and 5.

Chapter 2

Computational Methodology

Traditionally, experiments used to play the key role in finding and characterizing new materials. However, experimental research must be conducted over a long time period for an extremely limited number of materials and it imposes high requirements in terms of resources and equipment. Alternatively, computational studies enabled researchers to explore the materials and characterize them more efficiently.

In this thesis, we implement different computational simulations to understand the fundamental thermodynamic forces and mechanisms leading to the observed structures, and to process and study the optimum structures possessing the most desirable properties of interest. These methods provide us efficient modeling of materials which gives deeper insights into the structural characterization. In the following sections, we describe an overview of these methods.

2.1 Molecular Dynamics

Molecular Dynamic (MD) simulations [18] are used widely as a method for analyzing the movement of atoms, in which the simulation numerically solves Newton's equations of motion [19], thus allowing structural fluctuations to be observed with respect to time. MD simulation affords thermal averages of molecular properties and according to the ergodic hypothesis [20], we can simulate a single molecule with its surroundings for a period of time and get time-averaged molecular properties that approach the experimentally measurable ensemble averages. In order to calculate the microscopic behavior of a system from the laws of classical mechanics, MD requires a description of the interaction potential (or force field) as an input. The forces between atoms can be either computed from first principles by solving Schrödinger's equation, or approximated using a system of non-linear responses to fit the empirical data. The use of empirical potentials allows for faster calculations following only specific atomic degrees of freedom, hence larger and more complex systems can be treated by allowing some reduction in accuracy. In general, the quality of the results of a MD simulation depends on the accuracy of the description of these inter-particle interaction potentials.

In our research, MD simulations are employed to study the effect of temperature on the properties of our crystalline and amorphous structures. The computed results can therefore be optimized to estimate macro-scale properties based on the appropriate periodic boundary conditions. In amorphous structures, nearly half the atoms are on the outer faces, and these will have a large effect on the measured properties. Surrounding the box of atoms with replicas of itself takes care of this problem which can be applied by using the periodic boundary conditions in MD simulations. All MD simulations in our study are carried out using the Large-scale Atomic/Molecular Massively Parallel Simulator package (LAMMPS) [21].

2.1.1 Inter-atomic Potentials

In Molecular Dynamics, inter-atomic interaction rules must be defined and the quality of the results of a MD simulation depends on the accuracy of the description of these inter-particle interaction potentials. In general, the potentials should accurately describe the interactions between atoms and transferability and computational efficiency should be considered as well. For example, when dealing with large systems, computational speed is important and simple potentials can be used; and when finer levels of detail are needed, potentials based on quantum mechanics are used. The potential energy between N particles can be developed into terms that depend on individual atoms, pairs, triplets and so on:

$$\vec{U}(r_N) = \sum U_1(\vec{r}_i) + \sum \sum U_2(\vec{r}_i, \vec{r}_j) + \sum \sum \sum U_3(\vec{r}_i, \vec{r}_j, \vec{r}_k) + ... \tag{2.1}$$

where $r_N = (\vec{r}_1, \vec{r}_2, ..., \vec{r}_N)$ stands for the complete set on $3N$ particle coordinates and U_1 is associated with a one-body term due to an external field or boundary condition, U_2 corresponds to a two-body term or pair-potential and it depends on the distance between the atoms without taking into account other atoms. U_3 is related to a three-body term, where the interaction of a pair of atoms is modified by the presence of a third atom.

Morse Potential:

To obtain the potential functions for a particular system, a functional form for the potential function can be assumed and the parameters to reproduce a set of experimental data can be adjusted. The potential functions representing the non-bonded energy are formulated as a sum over interactions between the particles of the system. The simplest choice, employed in many popular force fields, is the pair potential, in which the total potential energy can be calculated from the sum of energy contributions between pairs of atoms. In Morse potential [22], mainly pair-wise interactions are considered because this contribution is the most significant. Therefore, based on equation 2.1, the total potential energy of the system of N atoms interacting via pair potential can be defined as:

$$\vec{U}(\vec{r_1}, \vec{r_2}, ..., \vec{r_N}) = \sum \sum U_2(r_{ij}) \tag{2.2}$$

where r_{ij} is equal to $|\vec{r}_i - \vec{r}_j|$.

In Morse potential specifically, the pair potential energy of two atoms i and j separated by a distance r_{ij} is defined as:

$$\phi(r_{ij}) = D[\exp(-2\alpha(r_{ij} - r_e)) - 2\exp(-\alpha(r_{ij} - r_e))] \tag{2.3}$$

where D and α are constants and have dimensions of reciprocal energy and distance, respectively and both of these parameters are determined empirically for every element. The parameter r_e is the equilibrium distance between the two atoms i and j.

Embedded-Atom Method Potential:

Daw and Baskes [23] developed the embedded-atom method (EAM) to describe the atomic bonding based on density functional theory. EAM is a semi-empirical method which is an intermediate trade between simple Morse potential and realistic ab-initio simulations. In the EAM, each atom is viewed as being embedded in the background electron density provided by neighboring atoms. Thus, the potential energy of a set of atoms is the summation of the pair interaction energy between nuclei of atoms i and j and the embedding energy as a function of the local background electron density around the ith atom. The total energy based on density functional theory can be defined as:

$$E_{TOT} = \sum F_i(n_i) + \frac{1}{2} \sum \Phi_{ij}(r_{ij}) \tag{2.4}$$

where $n_i = \sum \rho_j(r_{ij})$ and $\Phi_{ij}(r_{ij})$ is the pair potential term with the electrostatic core-core repulsion. $F_i(n_i)$ is also representing the energy won by the ion when it is embedded in the local electron density.

EAMs are widely used in molecular dynamics simulations and they are particularly appropriate for metallic systems.

2.1.2 Thermodynamic Ensembles

A thermodynamic ensemble is a statistical ensemble that is in statistical equilibrium which enables deriving the properties of a real thermodynamic systems from the laws of classical and quantum mechanics. We can consider different systems with different degrees of separation from their surroundings by imposing the thermodynamics constraints. For molecular dynamic simulations, three main ensembles will be considered.

NVE ensemble (Microcanonical): If a system is ergodic, average quantities computed along the trajectory generated by a MD simulation at constant number N of particles, volume V and total energy E, are equivalent to ensemble averages in the microcanonical ensemble. Usually numerical integration of equation of motions in MD is accomplished using Verlet algorithm [24]. In other words, if all the forces in the Newton equation of motions are related to the potential energy of the system, then the total energy of the system is conserved [25]. If the total number of atoms N and the volume V of the unit cell are also kept constant, then the MD simulations are performed in the microcanonical (NVE) ensemble; thereafter the NVE ensemble can be used to analyze an isolated system in equilibrium.

NPT ensemble (Isothermal-isobaric): In this ensemble, although the energy can transfer across the boundary, the matter cannot transfer. As opposed to the NVE ensemble, the volume of the system can change such that the internal pressure of the system matches the external pressure so that the pressure (P) remains constant. The system also should be in contact with a heat source that maintains a controlled and fixed temperature of T, and at the same time, the number of particles (N) remains constant as well [26]. The isothermal-isobaric ensemble is important when attempting to describe the Gibbs free energy of a system, which is the maximum amount of work a system can do at constant pressure (P) and temperature (T).

NVT ensemble (Canonical): In the canonical ensemble, similar to the NPT ensemble, energy can transfer across the boundary between the system and surroundings, but matter cannot. Also the system and the surroundings should be in contact with the heat source, so that the system will transfer heat (q) to and from the surroundings until the system and the heat source are in thermal equilibrium. In this ensemble, the number of particles (N) and the total volume of the system (V) remain constant. As described in the microcanonical ensemble, the total energy is fixed, but in the canonical ensemble the energy is no longer constant and it can take on a range of values depending on the temperature. The canonical ensemble is specifically important when attempting to describe the Helmholtz free energy of a system [27], which is the maximum amount of work a system can do at a constant volume (V) and temperature (T) [28].

2.2 Density Functional Theories

In density functional theory (DFT) [29], the goal is calculating the electronic structure of atoms, and the materials' properties are coming from the fundamental laws of quantum mechanics. Using this theory, the properties of a many-electron system can be determined by using functionals, which can be further used for interpretation and prediction of complex system's behavior at an atomic scale. In this method, the atoms are moved according to the forces generated by the converged electronic density at each timestep and the functional is the electron density which is a function of space and time. The density functional theory calculations in this thesis are performed by the Vienna Ab-initio Simulation Package (VASP) [30].

2.3 Machine Learning Techniques

The establishment of a relationship between the properties and the structure of amorphous materials is of great importance. The advent of machine learning brings a new area for establishing relations where simple theory has previously been intractable. In recent years, the availability of large data sets combined with the improvement in algorithms and the exponential growth in computing power has led to the vast uses of machine learning techniques. The large-scale simulations and calculations together with experimental high-throughput studies are producing an enormous amount of data that can be analyzed by using machine learning methods. The representation of a material is a set of quantitative attributes that describe the material and is what serves as input to a machine learning model. The goal in selecting a representation for materials is to construct a set of attributes that both differentiates distinct materials and captures many physical factors that could correlate with the properties of interest. By including attributes that are known to be correlated with the property of interest as input into the model, it becomes easier for a machine learning algorithm to automatically recognize these correlations and, thereby, create a more powerful and predictive model. The benefit of machine learning is that the functional form which links these attributes to any material property does not need to be known beforehand and is recognized automatically. In this thesis, we focus on two different techniques: unsupervised and weak supervised learning. In what follows, we elaborate more on each technique.

2.3.1 Unsupervised Learning

In unsupervised learning, the algorithm infers patterns from a data set without reference to known, or labeled outcomes and builds a model that detects the underlying structure or distribution in the data in order to learn more about the data [31]. Among the unsupervised learning techniques, clustering allows us to automatically split the data set into groups according to similarity and in each group there is a set of objects in such a way that objects in the same group (called a cluster) are more similar to each other than to those in other groups [32]. We specifically leverage this technique when we do not have labels for data which is the case in identifying the defects in amorphous structures.

2.3.2 Weak Supervised Learning

Machine Learning techniques are used vastly; however, the real-world usefulness of these models are all depending on access to high-quality labeled training data. This need for labeled training data is a significant obstacle to the application of machine learning models. Also labeling the data is not always practical and cheap. Some data may also need relevant expertise or specific training and a huge amount of time in order to label the data appropriately. For this purpose, weak supervision learning can be used to eliminate the need of collecting ground-truth labels. Weak supervision learning is capable of providing supervision signals for labeling large amounts of training data These labels are imperfect, but can nonetheless be used to create a strong predictive model [33].

Using weak supervision, users can write noisy labeling functions to generate labels for their data [34]. These labeling functions are historically high in accuracy but may be low in coverage. In this thesis, a library called Snorkel [35] is implemented for the purpose of weak supervision learning. In Snorkel, the heuristics are called labeling functions and each labeling function labels a subset of data. These labeling functions are defined by the user and then fed into the model. Weak supervised learning uses a combination of two models: generative [36] and discriminative models [37]. The generative model assigns probabilistic labels to millions of data points using the labeling functions. Then these outputs from the generative model would be fed into a classifier, which can generalize beyond the reasons directly addressed by the labeling functions. In other words, by getting large volumes of lower quality supervision and using statistical techniques to deal with noisier labels, we can train a higher-quality and a more powerful model.

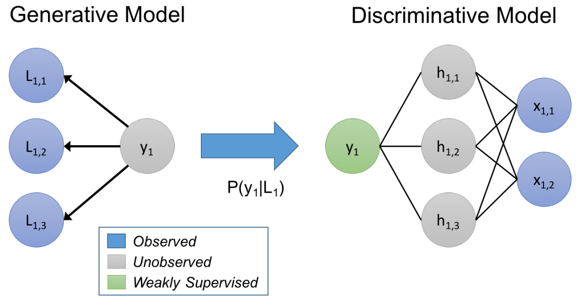

Figure 2.1: Weak supervised learning model: a combination of a generative and a discriminative model

The generative model in weak supervised learning provides us the opportunity for injecting our domain knowledge and heuristics which may guide our algorithm even if they might not be perfectly accurate. These heuristics (labeling functions) will produce noisy outputs which may overlap and conflict, producing proper training labels. However, in Snorkel, we have the opportunity to denoise the labels using the data programming approach, which comprises three steps:

The first step is applying the labeling functions that we defined to unlabeled data. These labeling functions labels a subset of our training data. For the next step we use a generative model to learn the accuracies of the labeling functions without any labeled data, and weight the outputs accordingly. We can even learn the structure of their correlations and dependencies automatically. This generative model outputs a set of probabilistic training labels, which we can use for the last step to train a powerful, flexible discriminative model (such as a neural network) that will generalize beyond the signal expressed in our labeling functions. Then for any other data set, we can employ this discrimitive model to obtain the outputs for the target labels. This whole pipeline provides a simple, robust, and model-agnostic approach to finding the patterns and label the training data.

Chapter 3

Analysis

In this chapter, we cover all the metrics and methods that have been used to measure and describe the properties in amorphous and crystalline materials in this thesis. These quantitative properties provide us insights into the materials' properties, characteristics, packing configurations and distribution of atoms and effectively describe how an atomic structure is transformed into a numerical representation.

3.1 Voronoi Volume

The voronoi method is a widely used method to determine the coordination number, in which, three dimensional space is divided into cells centered by atoms. A plane is drawn to bisect each line connecting the central atom and one of the neighboring atoms, and the cell surrounded by all such planes is called a voronoi cell [38]. This method is used for analysis of particle systems, for tracking changes in density, and for examining

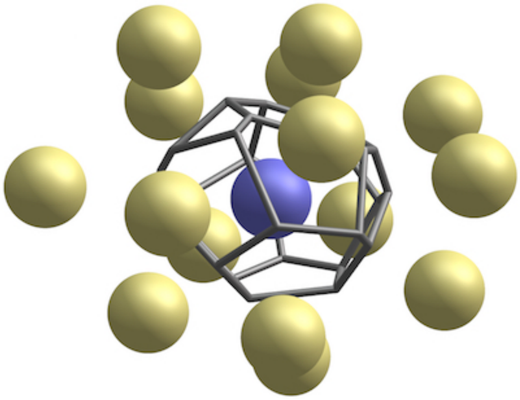

Figure 3.1: Voronoi cell

local neighbor relationship. Based on voronoi calculations, we can also determine the free volume of each cell which is basically obtained by subtracting the atom volume from the voronoi volume. Calculations for the voronoi cells are performed by the program called Voro++ [39].

3.2 Packing Correlation

For analyzing the internal structure of the amorphous structures and gaining information about the local packing behaviour in these materials, packing correlation metrics are helpful. Packing correlations provides us useful information about how the atomic spheres are distributed within a unit cell. Some of these packing correlation metrics are described below.

3.2.1 Cluster Packing Efficiency Attributes

Cluster packing efficiency attributes are based on the hypothesis that the system is composed of special arrangements of atoms that are both energetically stable and symmetrically incommensurate with long-range order [40]. We use these special clusters to calculate where the ratio between the radius of the central atom and the average radius of the first neighbor shell (r_{mean}) is close to the ideal ratio for a cluster of size (r^*). The ideal ratio is determined by the number of atoms in the cluster, similar to Pauling's rules for ionic crystals [41]. This packing efficiency of a cluster can be characterized by the Atomic Packing Efficiency (APE) measure, ($\frac{r_{mean}}{r^*}$), which is equal to 1 if the cluster is ideally packed.

3.2.2 Nearest Special Clusters

In nearest special clusters, the first step of the calculation is to determine the compositions of the clusters by finding all the possible clusters whose Atomic Packing Efficiency (APE) is between 0.99 and 1.01. Specifically, we search through all clusters in a range of numbers of atoms composed of any number of each element in the system. To generate attributes, we compute the mean Euclidean distance between the composition of each system and a few of these special clusters which are closest in composition to the alloy. The idea behind this method is closed to K-mean clustering machine learning technique [42].

3.2.3 Mean Packing Efficiency

Mean Packing Efficiency is a measure of the expected packing efficiency around all atoms in a structure. It basically provides information about the average of total space in a unit cell that is filled by the constituent particle. We can compute the optimal APE of a cluster where the central atom is one of the elements presented in the system and the composition of the neighboring atoms is equal to composition in the system, and then we select the number of atoms in the neighbor shell which produces an APE closest to 1. The composition constraint ensures all atoms in the material can form an interpenetrating network. We then select the number of neighboring atoms in the cluster that yields an APE closest to 1. We repeat this process for each type of atom in the system (e.g., for the bulk metallic glass of AMZ4, we determine the optimal Cu-centered, Zr-centered, Al-centered and Nb-centered clusters). Then, we compute the composition-weighted mean of the APEs and the mean absolute deviation of the APEs from 1.

3.3 Centro-Symmetry

The centro-symmetry parameter is used to characterize the degree of inversion symmetry in each atom's local environment [43, 44]. The centro-symmetry parameter is able to measure the local lattice disorder around an atom and can be used to characterize if an atom is part of a perfect lattice, a local defect or at a surface. Centro-symmetry parameter can be computed with the following formula:

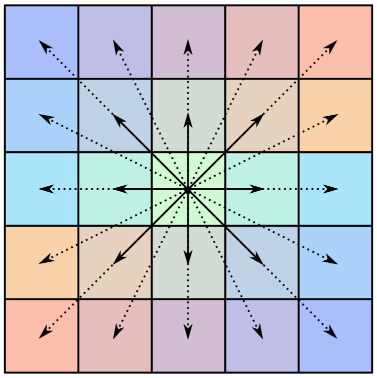

Figure 3.2: Centro-symmetry, a measure of inversion.

$$CS = \sum_{i=1}^{\frac{N}{2}} |\vec{R}_i + \vec{R}_{i+\frac{N}{2}}|^2 \tag{3.1}$$

where N is the number of atoms in the nearest neighbors for each central atom and R_i and $R_{i+\frac{N}{2}}$ are vectors from the central atom to a particular pair of nearest neighbors. This parameter can give us useful information about the arrangement of atoms and it is a measure of inversion symmetry (how there is an indistinguishable point for every point in the unit cell). This metric can be used to shed light on local inversion-symmetry in the random structure of amorphous systems.

3.4 Pair Distribution Function

Pair distribution functions (PDFs) possess useful local atomic pair and structure information, such as the distances between central and neighboring atoms and the nature of neighboring atom.The PDF can be used as a method to analyze the data and investigate the change in local atomic packing configurations [45, 46]. In general, PDF describes how, on average, atoms in a system are radially packed around each other. The pair distribution function is defined as:

$$g(r) = \frac{\rho(r)}{\rho_0} \tag{3.2}$$

and as a simpler form, it is calculated based on the number of atoms per unit of the shell volume:

$$g(r) = \frac{N\big(r \pm \frac{\Delta r}{2}\big)}{V\big(r \pm \frac{\Delta r}{2}\big)} \tag{3.3}$$

And the companion function to $g(r)$, total reduced pair distribution function $G(r)$, which is related to the total PDF and the total pair density function $\rho(r)$ is defined by:

$$G(r) = 4\pi r(\rho(r) - \rho_0) \tag{3.4}$$

in which, $\rho(r)$ represents the atomic pair-density, ρ_0 is the average atomic number density and r is the radial distance, $N\left(r \pm \frac{\Delta r}{2}\right)$ is the number of atoms within the shell and $V\left(r \pm \frac{\Delta r}{2}\right)$ is the volume of the shell. The major contribution to $G(r)$ is the atomic spatial correlation of the majority atomic species which have large scattering lengths.

Experimentally, the pair distribution function can be obtained by X-ray diffraction experiment after Fourier transformation [47] (also known as total scattering analysis). The degree of order is given by the sharpness of the peaks meaning that in crystals, the higher order of atoms leads to sharper peaks comparing to amorphous structures, where peaks occurring at distances of one to two bond lengths represent short-range order (around 4 Å-6 Å) and distances of three to four bond lengths represent medium-range order (around 8 Å- 10 Å) [48]. On the other hand, the intensity of peaks in $G(r)$ represent the probability of finding a pair of atoms with a separation of r, compared to the average atomic number density in the sample. This method can effectively characterizes the distribution of distances between pairs of atoms in our amorphous structures.

3.5 Smooth Overlap of Atomic Potentials

The local environment of each atomic species in the system can be described by using the smooth overlap of atomic potentials (SOAP) structural descriptor. SOAP relies on a Gaussian smeared atomic density based on spherical harmonics and radial basis function. Integrating the atomic positions would need a lot of basis functions as they are point objects

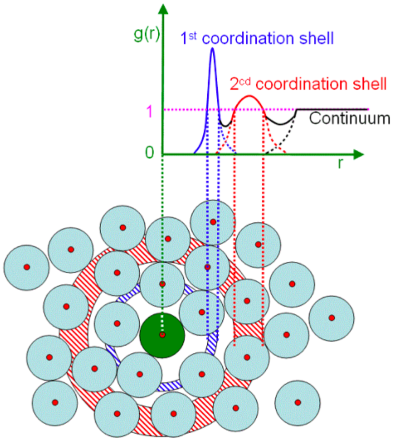

Figure 3.3: Mapping the environment of spheres to the pair distribution function

in space [49, 50]. Thus, in SOAP, the atoms' positions are smeared as gaussian functions in a way that SOAP for individual elements in the system is calculated and then, the values are concatenated at the end. Gaussian calculation on each local neighbor of a specified atom i is defined by:

$$\rho_i(\vec{r}) = \sum_j e^{-(\vec{r}_{ij}-\vec{r})^2/2\sigma_{atom}^2} f_{cut}(|\vec{r}_{ij}|) \tag{3.5}$$

where $\vec{r_{ij}}$ is the vector from atom r_i to r_j and f_{cut} represents a smooth cutoff function that ensures compact support at a cutoff distance. The Gaussians are defined as the species independent neighbor density of i. The Gaussian smoothed atomic density in the radial basis function form is defined by:

$$\rho_i(\vec{r}) = \sum_{nlm} c_{i,nlm} g_n(r) Y_{lm}(r) \tag{3.6}$$

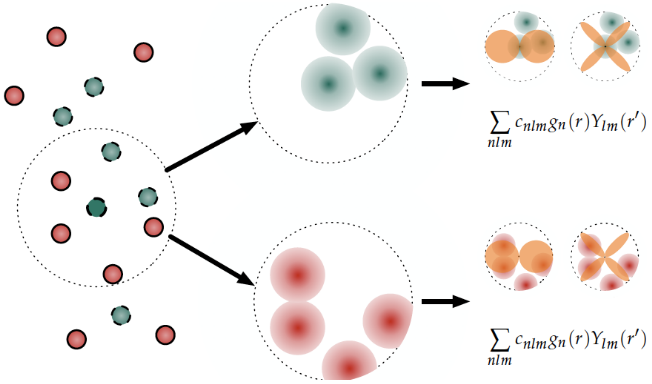

Figure 3.4: SOAP, the density around each atom is expanded into radial and spherical harmonics basis functions.

where Y_{lm} is spherical harmonics, $c_{i,nlm}$ is the expansion coefficient and g_n is an orthonormal radial basis. The SOAP kernel between two atomic environments can be retrieved as a normalized polynomial kernel of the partial powers spectrums which is:

$$K^{SOAP}(\rho_i, \rho_k) = \left(\frac{\rho_i \cdot \rho_k}{\sqrt{\rho_i \cdot \rho_i \rho_k \cdot \rho_k}} \right)^{\epsilon} \tag{3.7}$$

We raise the function to a power $\epsilon > 1$, in order to sharpen the difference between atomic environments. The SOAP calculations in this thesis are all carried out by a python library called DScribe [51].

3.6 Local Many-body Tensor Representation

Local Many-body Tensor Representation (LMBTR) encodes a structure by using a distribution of different structural motifs for each local environment and the distribution of atoms is constructed based on the kernel density estimation. The kernel density estimation enables representing the structure by distribution of scalar values which are the result of applying transformation on a chain of atoms. For describing the geometric features of atomic system, we define:

$$f_k(x, z_1, .., z_k) = \sum_{i_1,...,i_k} w_k \mathcal{N}(x|g_k) \prod_{j=1}^{k} \delta_{z_j}, z_{ij} \tag{3.8}$$

where in (3.8), g_k is a k-body function, $\mathcal{N}(x|\mu)$ denotes a normal distribution with mean μ evaluated at x and w_k is a weighting function that reduces the influence of atoms far from each other. Also the product of Kronecker δ-functions restricts to the given element combination $z_1, ..., z_k$. The LMBTR calculations in this thesis are also performed by DScribe package [51].

3.7 Bond-Orientational Order

This approach is commonly used to identify icosahedral ordering in an ensemble generated by molecular dynamics simulations and it focuses on the orientation of bonds from a central atom to the surrounding nearest neighbor atoms [52]. The bond orientations are expressed in terms of spherical harmonics, $Y_{lm}(\theta, \phi)$, where θ is the polar angle and ϕ denotes the azimuth angle in the reference system. The specific bond-orientational parameter is calculated from the sum over all the nearest-neighbor bonds, N_b, and is defined by:

$$q_{lm} = \frac{1}{N_b} \sum_{j=1}^{N_b} Y_{lm}(r_{ij}) \tag{3.9}$$

Since some equivalent structures may be oriented differently and thus counted as different, the rotational invariant combination is used to compute the correct bond orientational parameter

$$Q_l = \sqrt{\frac{4\pi}{2l+1} \sum_{m=-1}^{l} |q_{lm}|^2} \tag{3.10}$$

3.8 Thermal Properties Calculation Methods

As a part of this thesis, we study the heat transport of a crystalline structure ($LiAlO_2$) and the effect of different types of defects on this physical property. For this purpose, the thermal conductivity of the system is calculated via two different methods: Green-Kubo (Equilibrium method) and Muller-Plathe (non-equilibrium method). The details of each of these methods are represented in the remaining part of this chapter.

3.8.1 Green-Kubo

Green and Kubo proved that the coefficients describing the transport properties of the system can be represented as integrals of auto-correlation functions. Green-Kubo analysis is a method to decompose the heat flux into the time derivative of normal mode coordinates in order to calculate the thermal conductivity. By using the fluctuation dissipation theorem, the Green-Kubo method correlates the thermal conductivity tensor to the heat current tensor for equilibrium fluctuations. This method is based on the analysis of the auto-correlation function of the microscopic heat current derived by Kirkwood. Usually in calculations by the Green-Kubo formula, only nearest neighbors interactions are considered directly because accounting for the long-range interactions in simulations is computationally expensive. According to the Green-Kubo formalism, the thermal conductivity tensor is given by:

$$k_{\alpha\beta} = \frac{V}{k_B T^2} \int < J_\alpha(t+t^{'}) J_\beta(t) > dt^{'} \tag{3.11}$$

where α and β represent cartesian directions, V is the volume of the system and k_B is the Boltzmann constant. Also T is the temperature of the thermal equilibrium and angled bracket notation denotes the ensemble average. J is the heat flux and defined by:

$$J(t) = \sum_i v_i \epsilon_i + \frac{1}{2} \sum_i \sum_{j,i \neq j} r_{ij}(v_i.F_{ij}) \tag{3.12}$$

where v_i is the velocity of a particle i, F_{ij} is the force acting on atom i due to existence of atom j, and ϵ_i is the microscopic site energy of atom i.

GK calculations have the advantages of weak system-size dependence and full anharmonicity, and can be applied to both crystal and disordered systems with arbitrary temperatures, which is the case in this thesis [53, 54, 55].

3.8.2 Muller-Plathe

A non-equilibrium molecular dynamics method to implement for calculating the thermal conductivity in materials is Muller-Plathe (MP) method. In contrast to other non-equilibrium schemes, this method is not time-reversal invariant. The basic idea behind MP method is that first we induce a temperature gradient or heat flux and then we monitor the quantity of temperature gradient. Before we start, we divide the simulation system into N layers, and then the heat flux is imposed along one direction (here assuming z direction), causing the system to have temperature gradient as a response to this heat flux. In this situation, the hottest atoms and the coldest atoms exchange their velocity which induces a temperature ingredient in the system [56, 57]. Base on this, the thermal conductivity then can be calculated by:

$$\lambda = d\frac{j_z}{\Delta T} \tag{3.13}$$

where ΔT is the temperature difference and the heat flux j is defined by the sum of exchange energy per unit area and time as followed:

$$j_z = \frac{1}{2tA}\sum \frac{m}{2}(v_{hot}^2 - v_{cold}^2) \tag{3.14}$$

where m is the atomic mass, v_{hot} and v_{cold} represent the velocities of the hottest and coldest atoms to be exchanged at each step, t is the simulation time and A is the cross-sectional area of the simulation system perpendicular to the heat flux direction z, the mechanism of heat flux and thermal conductivity calculation is shown in the figure 3.5.

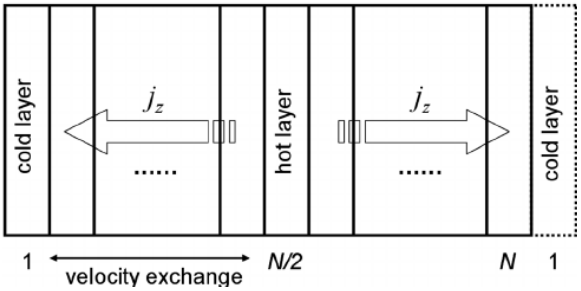

Figure 3.5: MP method of thermal conductivity calculation.

In MP method, since there are no sources of energy in the intervening slabs, the steady-state heat flux is the same for all of the layers. This implies that thermal conductivities for several intermediate temperatures and densities can be efficiently calculated from the local temperature gradients.

Chapter 4

Fragility in Glass-Forming Liquids

In this chapter, we are characterizing thermodynamically-driven changes in liquid structures, and quantifying the degree of amorphousness in metallic forming liquids. We also discover the dynamics of the liquids by seeking the viscosity-temperature relationships while approaching the glass transition. This relationship hints at the phenomenon of fragility. In this study, we quantitatively link atomic scale structure to fragility in the super-cooled liquid state (above the glass transition zone).

Fragility in a liquid refers to the sensitivity of its bonding network and is associated with non-Arrhenius dependence of the liquid's viscosity as it approaches the glass transition temperature. In bulk metallic glasses (BMGs), ductility in the glassy state correlates with fragility of glass forming alloys in their molten state, so understanding the origins of fragility could provide insights into plasticity mechanisms in BMGs. The phenomenon of fragility in a liquid is the non-Arrhenius change of kinetic properties such as viscosity with temperature and basically is defined based on the deviation of the temperature dependence of a liquid's viscosity from Arrhenius behavior. It means that the structure of the liquid—the bonding and packing environment experienced by its atoms— changes with temperature, and thus the activation energy for the atoms to move past one another also changes with temperature. In other words, the adjective fragile here is referring to the sensitivity of the liquid's bonding network to temperature.

4.1 Background

As discussed, kinetics of the liquid can be described by the concept of fragility and fragility of a liquid reflects the sensitivity of the viscosity of the liquid to temperature changes and it is found to be an important consideration in the design and structural performance of bulk metallic glass forming alloys. Moreover, the properties like fracture energy, ductility and plasticity of the glass is related to the kinetics defined by fragility of its glass-forming liquid. Understanding the underpinning causes of fragility can provide strategies for designing new BMGs with improved ductility. Additionally, the geometric effect or, more specially, atomic size effect contributes to the easy formation of BMGs. Numerous relations and theoretical fragility calculations have been suggested for the possible parameterizations and calculations of the temperature dependence of viscosity and understanding the origin of fragility. For example, S Sastry [58], Aleksandra Drozd-Rzoska et al. [59], and Isabella Gallino [60] started from thermodynamic considerations using the Adam–Gibbs equation for entropy to formulate an analytical model of viscosity-temperature relationship, which seems to fit many glass-forming liquids quite well. They analyzed the relationship between fragility and quantitative measures of the energy landscape and proved that fragility depends on changes in the vibrational properties of individual energy minima in addition to their total number and spread in energy. This thermodynamic expression for fragility provides physically reasonable and realistic values at low- and high-temperature scaling of viscosity. It is also in quantitative agreement with kinetic fragilities obtained from the liquid's diffusivity.

Also David L. Sidebottom [61], C. Yildirim et al [62] , Mark Wilson and Philip S. Salmon [63], by using molecular dynamic simulations, have found that the relaxation behavior of the super-cooled liquid is strongly correlated to the variation of network rigidity with temperature and the spatial distribution of the corresponding topological constraints. They consider the role of network topology in determining the fragility in network-forming oxide glasses. Fragility follows a very common dependence on the topological connectivity of the network provided this connectivity is adjusted to reflect the presence of larger-scaled rigid structural units that form in some systems. Then based on the thermodynamic expression of fragility, they explain how fragility is a reflection of the sensitivity of the network's configurational entropy to small changes in network connectivity of weakest links.

One simple necessary but not exclusive condition noted by Shuai Wei et al [64] is that the curvature of the enthalpy curves on a reduced temperature scale near T_g correlates with fragility in bulk metallic glass-forming liquids, and basically a more fragile system has a larger curvature which is caused by a slower non-equilibrium relaxation shortly before returning to equilibrium. This study was performed using the heat flow of differential scanning calorimetry during the glass transition. This observation also supports the behavior of theoretically calculated enthalpy curves during quenching, via the enthalpy landscape approach. Supporting this idea, Jing Guo et al [65] proposed that by the combination of mismatch entropy and enthalpy of mixing we can evaluate the liquid dynamic fragility as these two factors determine the stability of the super-cooled liquid, as well as the difficulty of atomic rearrangements.

Additionally, it is widely believed that there is a connection between the glass forming ability and the liquid fragility. For example, K F Kelton [66] and Hajime Tanaka [67] proposed that short-range bond ordering in a liquid is one of the key physical factors controlling liquid–glass transition, glass-forming ability and fragility. Generally, the higher degree of short-range bond ordering leads to the increase in the interface tension between the crystal and the liquid, and the decrease in the thermodynamic driving force of crystallization. Based on this, they suggest that the icosahedral order increases gradually for strong metallic liquids, however, this order rises rapidly near the glass transition temperature in more fragile liquids. Therefore, the stronger tendency of short-range bond ordering makes a liquid stronger and leads to the better glass-forming ability. The better glass-forming ability comes from the large free-energy barrier for nucleation and slow translational diffusion in the super-cooled region which is directly connected to the viscosity-temperature relationship (fragility).

4.2 Introduction

Despite the vast number of literature on bulk metallic glasses, little is known about the structural characterization and varieties in liquids above glass transition temperature, specifically in super-cooled region. Super-cooled region is of great importance and utility to improve the performance of its glass, leading to the fact that the formation of glass has become a challenge in a variety of fields like optical sciences, biomedical and aerospace. Fragility defined by Angell [68] can be measured by the fragility index which characterizes the slope of the viscosity of a material with temperature as it approaches the glass transition temperature from above. Fragility is observed in different liquids such as metal-organic framework, polymeric, and inorganic glass-forming liquids [69]. In all of these liquids, it is important to quantify the degree of their fragility. For measuring the fragility, two different parameters can be defined and used:

- Kinetic fragility index: This parameter is more related to the dynamical behavior of the liquid and how fast the atoms are moving around each other [70, 71]. This fragility index is defined by the slope of the viscosity (η) in an Angell plot and calculated by:

$$m_k = \frac{d\log\eta}{d(\frac{T_g}{T})}\Big|_{T=T_g} \tag{4.1}$$

- Structural fragility index: The structural signature of fragility is identified as the temperature dependence of local dilatation on distinct key atomic length scales. By

> using this atomic scale structure, we can relate the fragility to a liquid's structure without referring to dynamics of the liquid. This is calculated by the peak positions coming from radial distribution function of the liquid [66].

Wei and collaborators [72] indicated that the structural evolution of various bulk metallic glass forming liquids can be quantitatively connected to their viscosity behavior in the super-cooled liquid near T_g. They determined the peak positions of the pair distribution function (PDF) for seven different BMG liquids resulting by In-situ synchrotron x-ray scattering measurements. It was shown that there is a significant structural change in the packing behavior of strong and fragile liquids in the length scale of their neighboring coordination shells. These changes in intermediate order are seen at a distance far beyond the range of a typical inter-atomic or next-nearest-neighbor bond lead us to wonder if this effect originates from the steric packing effects arising from atomic size-mismatch. In the next section, we attempted to address this question by performing MD simulations and then quantifying the super-cooled region of the glass-forming liquids.

4.3 Method

In order to understand the mechanism behind the fragility phenomenon, a series of MD simulations using LAMMPS package [73] were performed. In these simulations, known strong and fragile BMGs are utilized with their atomic sizes. However, the atom interactions have remained the same in the system and they are based on Cu-Cu interaction but with different sizes. These strong and fragile BMGs are represented by hypothetical alloys with the same mixture of atomic radii, but with all atoms interacting via the same bonding. Then, we study the kinetics and packing behaviour of these glass-forming liquids. Remarkably, these radii alloys display many of the signatures of fragility as their real-life counterparts.

To begin with, three hypothetical alloys were chosen to mimic the atomic size ratios and proportions of the well-known bulk metallic glass forming alloys AMZ4, Pt42, and Pt60. By Angell's definition, AMZ4 (Zr-based family of metallic glass) is a strong liquid, whereas Pt42 and Pt60 (Pt-based family of metallic glass) are fragile liquids. The composition of these alloys are different. AMZ4 is composed of 59.3% Zr, 28.8% Cu, 10.4% Al and 1.5% Nb. On the other hand, Pt42 comprises 42.5% Pt, 27% Cu, 21% P and 9.5% Ni; and Pt60 has 60% Pt, 16% Cu, 2%Co and 22% P. The kinetic fragility parameter (logarithms slope of viscosity) for Pt42 and Pt60 is 56.9 and 73.7, respectively; this is substantially different from AMZ4's fragility parameter which is 41.4 [72]. As it is shown in table 4.3, in particular, Pt42 and Pt60 systems have more atomic size-mismatches and higher atomic ratio comparing to AMZ4. Each of these alloy systems consist of 7528 atoms and the amorphous structure of these alloys is also shown in figure 4.1.

AMZ4	%	Atomic radius	Pt42	%	Atomic radius	Pt60	%	Atomic radius
Zr	59.3	1.55	Pt	42.5	1.47	Pt	60	1.47
Nb	1.5	1.45	Cu	27	1.35	Cu	16	1.35
Cu	28.8	1.35	Ni	9.5	1.316	Co	2	1.25
Al	10.4	1.25	P	21	1	P	22	1

Table 4.1: The components and the radius of the particles for AMZ4, Pt42 and Pt60

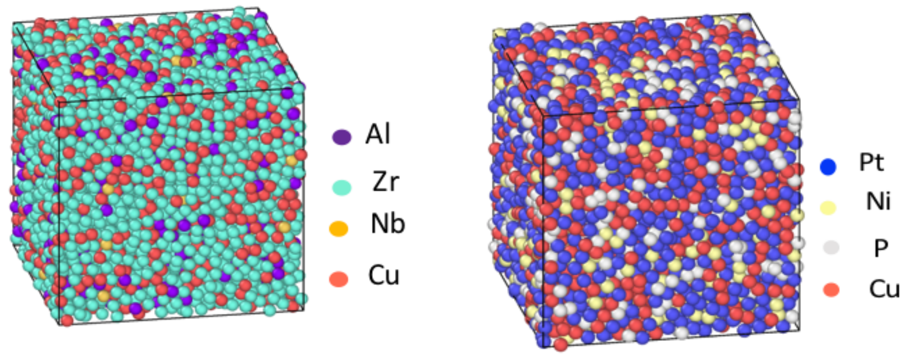

(a) (b)

Figure 4.1: The systems of amorphous BMGs (a) Zr-based metallic glass and (b) Pt-based metallic glass

4.3.1 Potential Energy

The choice of potential energy is important in this study as they directly affect the final calculations. For describing the interactions and bonding networks between the atoms, Morse potential was used. Morse potential is a proper inter-atomic interaction model for a potential energy of metals. It gives a more accurate and closer description of the dynamic behavior of glasses with spherical symmetry and simple mathematics, and it is adequate to analyze the behavior of atoms in the metallic state, where the bond is non-directional. Morse potential is popular for simulations of metals in our system as it allows us to use an analytical, computationally fast potential with realistic parameters and known anharmonicity (more details about this potential was discussed in section 2.1.1). Specifically, the anharmonic component of the Morse potential is different from that of other potentials, enabling us to check the influence of anharmonicity on the properties of the material and, in particular on its fragility.

In this study, we first tried EAM potential which is a more realistic potential energy for describing the interactions between the spheres. However, to extend the Cu-Cu interaction and make it applicable for the other pairs in the system, as we tuned the bonding parameters, the interactions were complex non-linear interactions. This resulted in challenges in tuning the atom sizes solely. Thus we continued with Morse potential. Each parameter for Morse potential was chosen based on the atomic interaction and the equilibrium distance was considered equal to the sum of two neighbor atoms' radius. By having different sizes of atoms packing together, the equilibrium distance between each pair of atoms was different.

As mentioned before, we are focusing on the effect of atomic-size mismatch on the fragility behaviour; therefore, to neglect the effect of potential interactions, we considered all the atoms are interacting with each other based on Cu-Cu interaction. In order to make the Morse potential between Cu atoms be applicable for the other species of atoms, we study two mechanisms for the potentials: (i) we set either the dissociation energy (which indicates depth) constant, or (ii) we set the force constant (which indicates curvature) for each pair of atoms, as shown in figure 4.2. Therefore, in our simulations, based on equation 2.3, we first considered D as constant, so the depth of the potential does not change. Secondly, α was considered to be constant, which means the curvature of the potential (the stiffness of the bonds) remains the same. The potential wells are different between two species; therefore, when Morse potential combines with a different potential well that has a different atomic radius, it creates better atomic packing and prevent the atoms from shrinkage. Thus, we stick to the potentials with the same curvature for the further simulations.

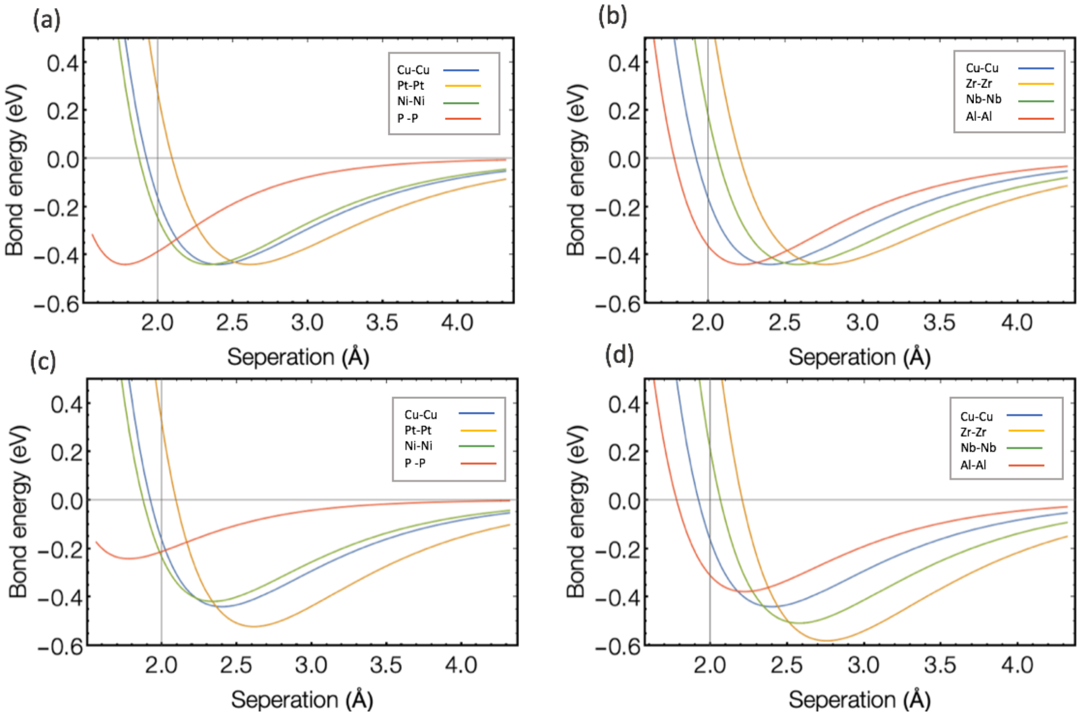

Figure 4.2: Morse potential with the same depth as Cu-Cu pair, for every pair of atomic interactions in (a) Pt42 and (b) AMZ4 metallic alloys, and also potentials with the same curvature as Cu-Cu interaction (same bond stiffness) in (c) Pt42 and (d) AMZ4.

4.3.2 T_g Calculation

After setting up the potential energy, as a starting point, it is important to calculate the glass transition temperature (T_g) for each BMG when focusing on the fragility of a super-cooled liquid region. Around T_g, as the liquid turns into the glass while cooling down the liquid, the changes in thermal properties such as density, viscosity and potential energy of the system are significant. The rate of $500Ks^1$ is the critical cooling rate meaning that it is the minimum cooling rate at which the liquid can form a glass without crystallization. The solidification starts at the glass transition temperature which causes a change in the behaviour of the thermal properties of the system. For example, the viscosity of the system rises enormously. Eventually, the super-cooled liquid will become so viscous that its volume will shrink at a slower rate, and finally it will become a seemingly rigid solid of glass [74, 75].

For determining the glass transition temperature, each alloy was heated up to reach a target temperature (1600 K), above the melting point. They were held at this temperature for 3 ns using nve ensemble to assure that the old configuration had disappeared. Then at different cooling rates of 1.2, 0.6, 0.4 and 0.24 Kps^{-1}, they were cooled down to the temperature much below the glass transition temperature (600 K) within npt ensemble. Fast cooling conditions are required to avoid crystallization during processing and basically if a liquid is cooled rapidly enough, so that the crystallization at or slightly below the melting point is avoided, the final state of the material will be an amorphous solid.

During this process of quenching, thermal properties like total energy, potential energy, and density were recorded. As discussed, around T_g, there is an abrupt change in thermal properties of metallic glasses which can determine the glass transition temperature. By plotting the thermal data and fitting curves on the cooling process plot, the average glass transition temperature for each alloy over all the different cooling rates was calculated. Calculated T_g for AMZ4, Pt42 and Pt60 is around 1150 K, 1200 K, 1210 K respectively. Figure

4.3.2 represents the thermal records of this process for Zr- and Pt-based alloys. The lower slope below the T_g is due to the lower heat capacity for the amorphous glass.

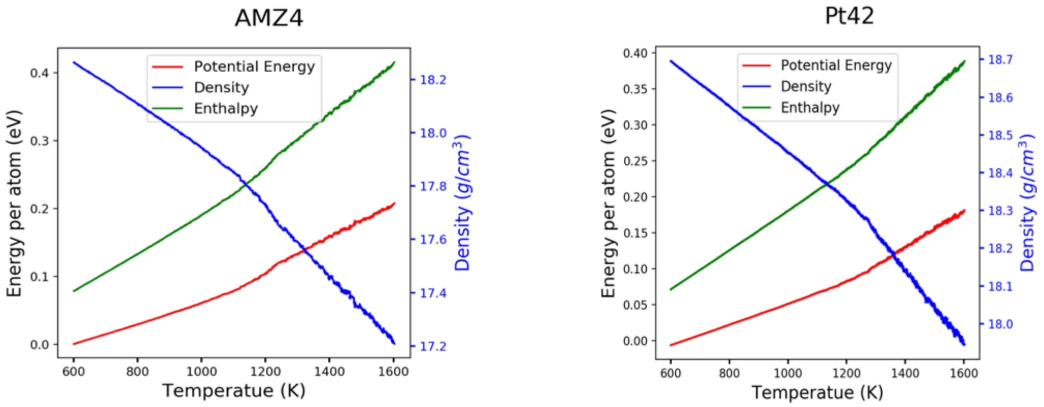

Figure 4.3: Thermal records of AMZ4 and Pt42 during quenching for the purpose of glass transition temperature calculation.

4.4 Characterization

For analysis of the internal structure of each glass as a function of temperature, alloys were held at 1600k for 5 ns where molten transition appeared and then they were cooled down to different temperatures above the T_g with the same previously mentioned cooling rates in npt ensemble. Then they were held at above T_g for a long time (around 15 ns). The average change of the potential energy for both alloys in this process of quenching is represented in figure 4.4. This figure shows how kinetics change as we approach the glass transition temperature in both glass-forming liquids. After holding the liquid systems for 15 ns in nve ensemble at different temperatures above the glass transition temperature, we reached the equilibrium state of the system. These final relaxed structures were then used for further analysis. As it is shown in figure 4.4, the relaxation of the potential energy is not the same in strong and fragile liquid. In Pt42 (fragile liquid), it takes longer for the atoms to rearrange and relax when compared to AMZ4 (strong liquid).

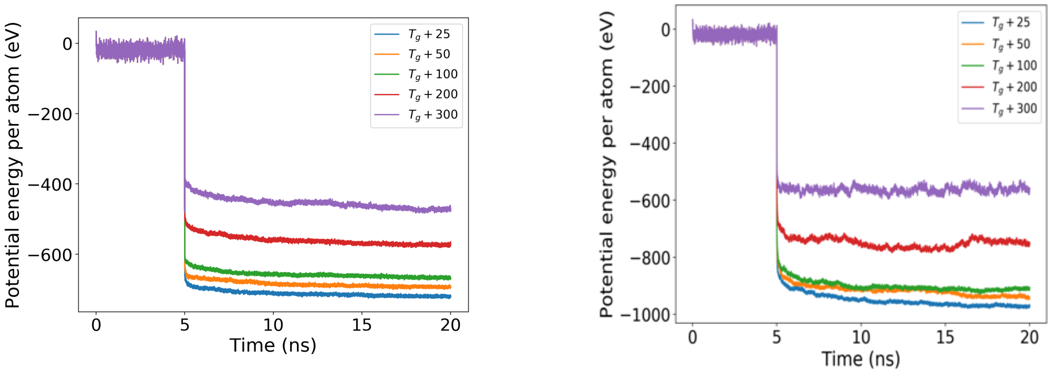

Figure 4.4: Energy relaxation of AMZ4 (on the left) and Pt42 (on the right) while quenching from the molten state of 1600 K to different temperatures above their T_g.

As there is not much information about the random structure of amorphous materials, a proper way to analyze their local packing behavior is by structural characterization, which is based on the simulations previously described.

In our simulations, PDFs can indicate if there is a connection between order of atomic changes in the structure and the kinetic viscosity in BMG liquids. The $G(r)$ of both glass-forming liquids based on the equation 3.4 was calculated at different temperatures.

Calculating the peak position changes in PDFs is considered a new way for figuring out the kinetics and packing configurations around the glass transition temperature. This method can represent the dynamic behavior of atoms around each other in super-cooled liquid region in short- and long-range orders. The position of the peaks for each PDF was carefully calculated by PDFs' derivative where the derivative is decreasing and crosses the value of zero (these calculations were coded in Python). The example of these calculations for PDF and its derivative for Pt42 at T_g+50 K is represented in figure 4.5. In the tail of the derivative figure, we can observe that a more dense number of peaks are recognized by our method and this is because the peaks are getting wider in further distances and thus, finding the exact position of the peaks is more challenging. However, since our focus in this study is on the short- and intermediate-range order (1st, 2nd, .., 5th peak), this method of finding peaks is successful in achieving our goal.

Now that we have calculated the peak positions, we can relate the structural changes to its kinetics and examine the peaks changes in each liquid based on the equation below:

$$\Delta r_i(T) = r_i(T_g) - r_i(T) \tag{4.2}$$

where $r_i(T_g)$ denotes the position of the ith peak at glass transition temperature, and $r_i(T)$ is the position of ith peak at a specific temperature. We calculated the average peak changes over the previous different cooling rates for all the 5 first peaks of the PDFs.

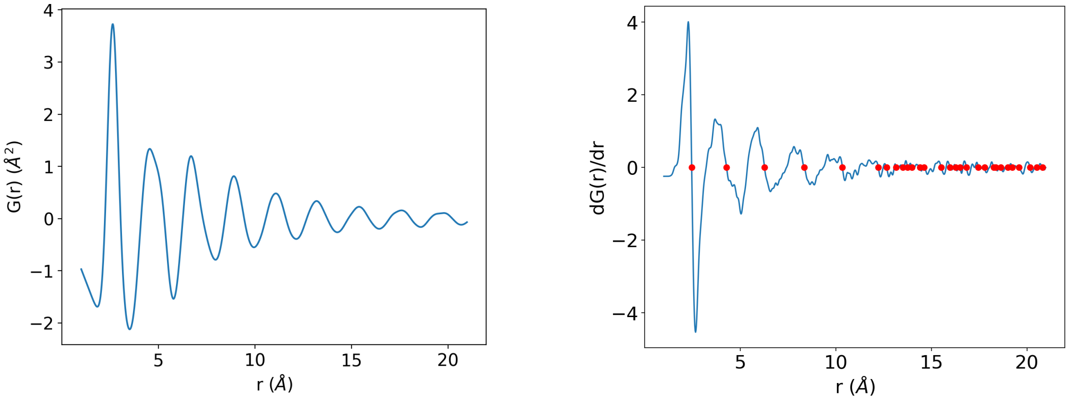

Figure 4.5: The $G(r)$ of Pt42 at 50K above its T_g and the corresponding derivative of $G(r)$ for determining the position of the peaks.

The results from calculating the first peak of the PDFs suggested that by increasing the temperature above T_g, the first peak shifts to left meaning that atomic clusters are packed more densely at higher temperatures. Ding et al [76] explained this shift by thermally redistribution of atoms based on the asymmetric property of inter-atomic potential. Furthermore, this may mistakenly be assumed that this shift to left means that the coordination number for the atoms is decreasing when we increase the temperature. However, we don't think this is the case. Because when increasing the temperature, the number of the neighbors are still the same. We believe this shift to the left is due to the artifact of $G(r)$ function. In $G(r)$, the atoms are rated by their distance from the central atom, this means that the neighbor atoms that are closer, have more contribution to $G(r)$ and the weight of this effect is $1/\mathrm{r}^2$. At higher temperature atoms are vibrating more, so the atom in the neighbor is still in the same coordination shell but because the guassians are weighted by r^2, the center of the sum of the guassians of these vibrations falls toward the centeral atom. So this is coming from the $G(r)$ equation even though the others have tried to explain this by physical properties which we think is wrong. We extended our calculations to the other peaks (2nd, 3rd, 4th and 5th) and we noticed that the ratio of the changes of the peak position for the first 3 peaks is more significant for the strong liquid; however, this trend changes for the fourth peak. Firstly, the fourth peak of the PDfs for our metallic liquids shifts to right, since the atoms have more degree of freedom to get further when increasing the temperature. Remarkably, the rate of the changes in the fourth peak of the fragile liquids was more distinguishable, suggesting that the thermally-induced spaces between the 3rd and 4th shells increased more significantly, causing the less denser packing of atoms and this is directly in connection with the greater changes of viscosity in fragile liquid, supported by Angell definition of fragility.

These findings are indicated in figure 4.6. The continuous lines are the results from our calculations, and the scatter plots are coming from the experimental data of the study by Wei and collaborators [72]. Although the trends of peak changes in fragile and strong liquids in this study is consistent with ours, the scale of the changes is different for two reasons: (i) the Morse potential energy that we defined brings different spacing within the atomic spheres and the thermal expansion of our systems is bigger (by a factor of 10) than the real alloys so we would underestimate the first peak. (ii) As we discussed, how the $G(r)$ is placing weights on distances of atoms can overestimate the peak positions. These two effects are in different directions, and as the second effect is greater in the near neighbor shells, leading to overestimating the first peak, and at further distances, since the effect of the thermal expansion dominates the effect of vibrations, we would underestimate the fourth peak change toward the central atom. If we cancel these effects, all the other contributions are coming from the structural changes.

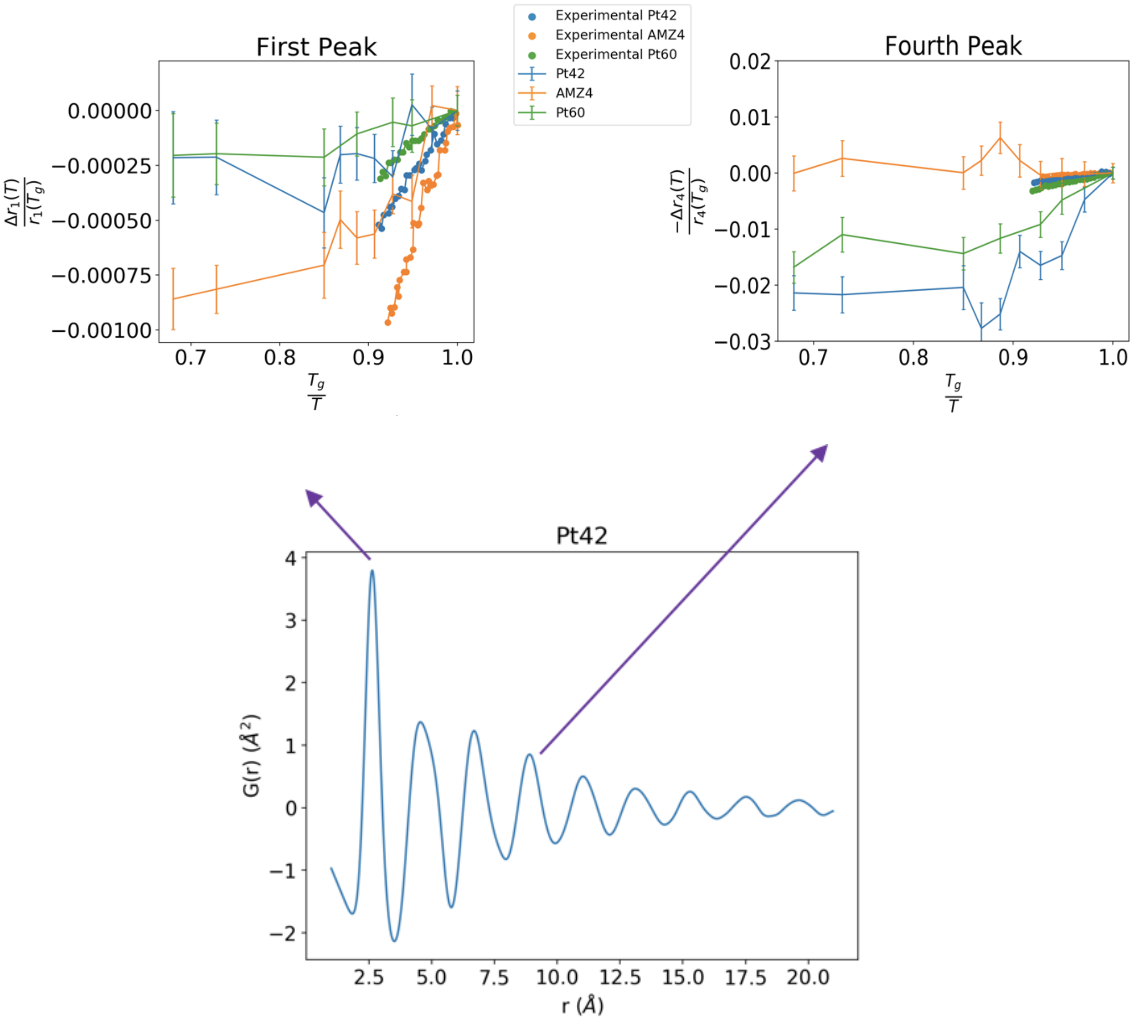

Figure 4.6: The first peak and fourth peak position changes in PDFs of fragile vs. strong liquids. The first peak changes for the strong liquid (AMZ4) is more pronounced when comparing to the fragile liquids (short-range order). However, this behaviour changes for the fourth peak positions(intermediate-range order.

In the random atomic order of a glassy solid, the atoms are packed less densely than in a corresponding crystal, leaving larger interstitial spaces, or holes between atoms. These interstitial spaces collectively make up what is known as voronoi volume, and they are responsible for the lower density of a glass as opposed to a crystal.

Resulting from the calculations, the voronoi distribution of metallic-forming liquids at different temperatures above the glass transition temperature is shown in figure 4.7. The voronoi distribution of the liquids exhibited a binomial distribution of volumes for Pt42 at the temperature around the glass transition temperature, whereas this behavior changes at higher temperature. This binomial distribution of voronoi in the fragile liquid is suggesting that most of the atoms are trapped at big cells, and at the same time, at smaller cells around T_g. At higher temperature the atoms rearranged and redistributed by the thermally induced energy, causing a more uniform distribution of their packing. They redistributed in a way to maximize their entropy, however, at lower temperature, the atoms pack together more efficiently leading to more bonds. And this is related to larger atoms being in neighbor of smaller atoms and vice versa, to maximize the packing efficiency. Since the interactions between atoms were the same in both alloys, this behaviour implies that the binomial distribution is coming from the atomic size mismatches existing in the systems.

As discussed in details in chapter 3, the centro-symmetry parameter is used to characterize the degree of inversion symmetry around each atom's local environment. The distribution of calculated centro-symmetry for both Pt- and Zr-based glass-forming liquids at different temperatures above T_g is represented in figure 4.8. Though the liquid alloys have different packing sizes, there is no obvious split in the behavior of centro-symmetry for each system, as observed in voronoi volume. However, the fragile liquid (Pt42) shows a narrower distribution of centro-symmetry, leading to a higher peak when compared to the strong liquid (AMZ4). The larger centro-symmetry means larger deviation from perfect symmetry arrangement of atoms, and the calculated centro-symmetry for these two liquids indicates that surprisingly, the symmetry is more broken around the atoms of AMZ4 comparing to Pt42, although this difference is not significant.

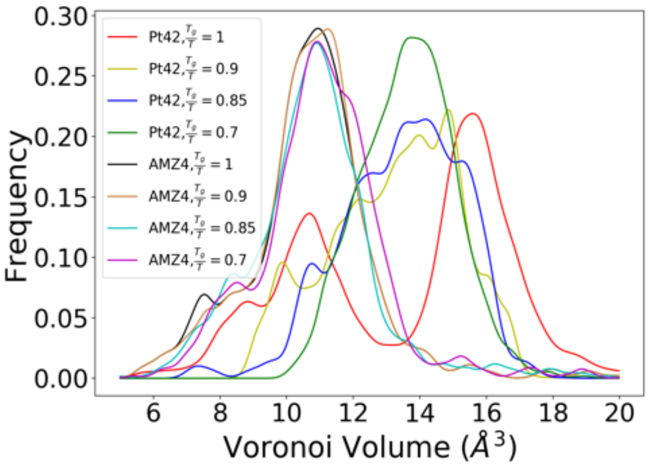

Figure 4.7: Voronoi distribution of Pt42 and AMZ4 at different temperatures.

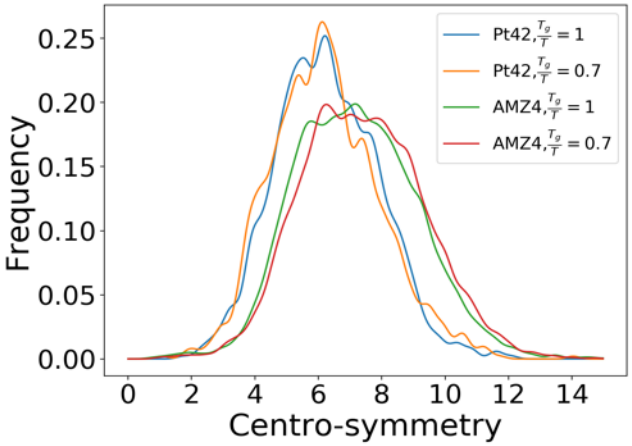

Figure 4.8: Centro-symmetry distribution of Pt42 and AMZ4 at different temperatures.

In the next step, we calculated the packing correlations for each species of atom in the system which gives us insights on the type of neighbor atoms around each central atom. This correlation for atom type B in neighbors of the atom type A in center can be calculated by:

$$PC_{AB} = \frac{AB\,pairs\#}{AX\,pairs\,\#} - f(A) \tag{4.3}$$

where AX denotes all pairs of atoms with species A in the center within the cutoff . Here $f(A)$ is the fraction of atom type A in the system. This metric basically provides insight into the correlation of a specific type of atom, be in the neighbor of another type of atom.

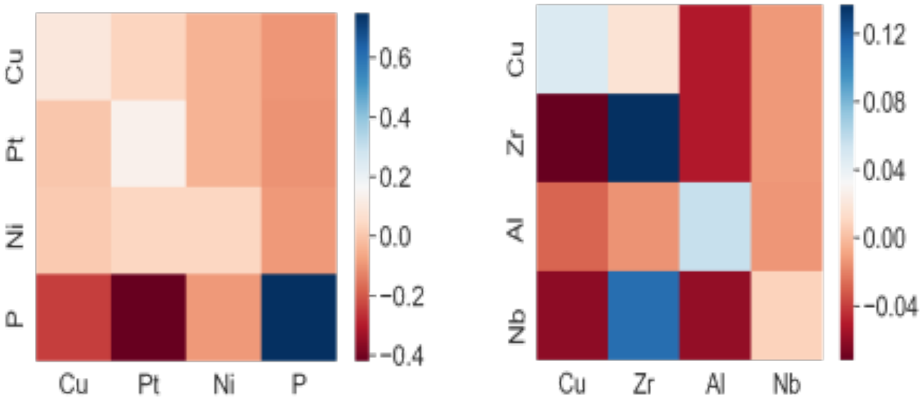

(a)

(b)

Figure 4.9: Packing correlation between each pair of atom species in (a) Pt42 and (b) AMZ4. The horizental axis belongs to the atom types in the center and the vertical axis belongs to the neighboring atom types.

The calculated packing correlation number around each atom specie of our fragile and strong liquids within a cutoff of 6 $\mathring{A}$ has been calculated and shown in figure 4.9. For example, in Pt42, there are more phosphorous atoms grouped around phosphorus than what expected. The range of deviations from the fraction ratio of atom species in Pt42 is larger than the one in AMZ4. Since we used the same number of the atoms in each system, meaning that the number of the bonds were the same; therefore, we expected that the packing correlations for each pair to be the same. However, calculated correlations have characterized different packing and structural behaviour in the liquids, which is coming from the packing effects of different sizes of atoms and extra degrees of freedom of spheres in the systems.

4.5 Configurational Entropy

In calculating the viscosity through kinetics, as mentioned before, we need a really long relaxation time which is not efficient computationally. Another way to look into kinetics by just looking at structures without recording the dynamics is through structural changes. These structural changes can be calculated through configurational entropy.

In a packing of poly-dispersed spheres, correlations between the arrangement of large and small spheres can lead to an increase in packing efficiency at the expense of configurational entropy. This would provide an entropic driving force for a change in structural configuration in a liquid with higher temperature caused by the atomic size mismatches. To analyze this effect, we calculated the configurational entropy of each glass-forming liquid at different temperatures.

The entropy can be calculated as a statistical quantity without reference to the underlying energetics that created the probability distribution [77]. The distribution function expansion first proposed by Nettleton and Green [78] can be expressed by:

$$\rho^2 \int_V g_N^{(2)}(r_1, r_2) dr_1 dr_2 = N(N-1) \tag{4.4}$$

The equation 4.4 is the expansion in grand-canonical ensemble with the double integral over positions r_1 and r_2 for N atoms in the volume V and density ρ where g is the positional correlation function. This equation can be expressed with two-body terms:

$$s_2 = S_{Fluct}^{(2)} + S_{Info}^{(2)} \tag{4.5}$$

In the above equation s_2 falls off rapidly in a way that the integrals sum converges faster when the range of integration extends to the large values of r. By separating each term, we define:

$$S^{(2)}_{Fluct} = \frac{1}{2} + \frac{1}{2}\rho \int (g(r)^2 - 1)dr \tag{4.6}$$

$$S^{(2)}_{Info} = -\frac{1}{2}\rho \int g^{(2)}(r) \ln g^{(2)(r)} dr \tag{4.7}$$

where the first term, $S^{(2)}_{Fluct}$, is coming from the fluctuations of N number of atoms and the other term, $S^{(2)}_{Info}$, is for making up the entropy reduction due to two-body correlation [79]. The calculation of these two terms, as well as the sum of them and also $G(r)$ for Pt42 at $T_g + 50$ K is demonstrated in figure 4.10. The calculated excess configurational entropy for each glass-forming liquid at temperatures above T_g is shown in figure 4.11. The different sizes of the atoms lead to different peak positions which results in the gap in entropy between the two alloys. To investigate more, we have broken down the total entropy into the contribution of each peak to this term. The configurational entropy in figure 4.12 (green line) has been scaled so that it converges to 1. This figure indicates that the major contribution to the excess entropy is coming from the first peak. Thus, the first neighbor shell of spheres is playing the key role in determining the entropy and differentiating the fragile and strong liquid.

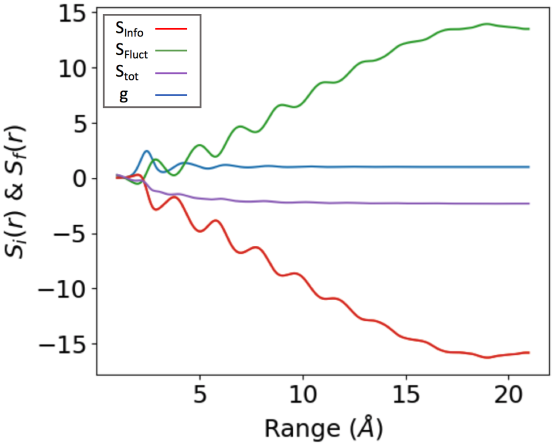

Figure 4.10: Two-body terms S_{Fluct} and S_{Info} and their sum from simulated pair correlation function for Pt42 at T_g+50 K.

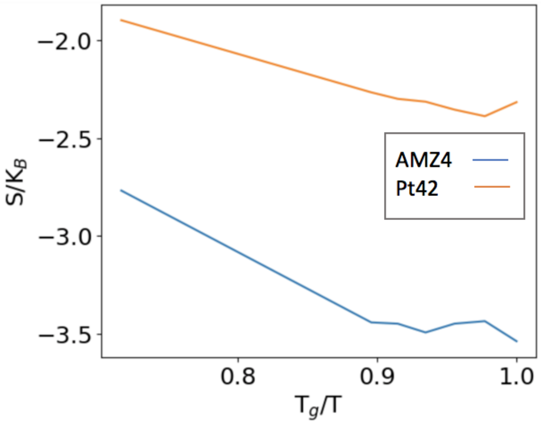

Figure 4.11: Excess configurational entropy for AMZ4 and Pt42.

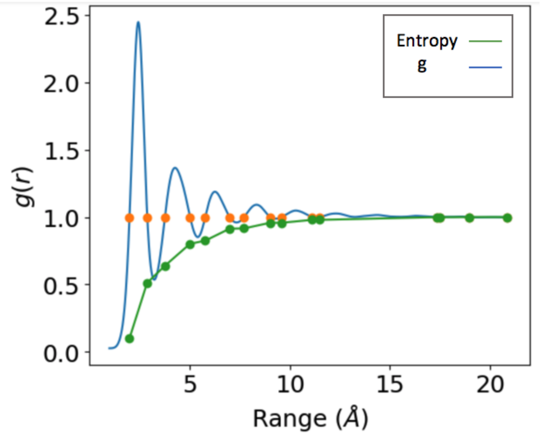

Figure 4.12: Contribution of each peak of $G(r)$ (blue line) to the configurational entropy of the system (green line).

4.6 Viscosity-Temperature Relationship

The transition of a liquid into a glass is controlled by the behavior of the viscosity as temperature decreases. Viscosity is the key parameter to describe the sluggish kinetics and dynamic behaviour in the molten super-cooled state. Measuring fragility is not an easy way, since we should calculate the viscosity. In Angell plot, we observed that the viscosity of the liquid changes by 5 orders of magnitude when approaching the glass transition temperature, and this means the relaxation time should be really long for our simulations which is not possible. This makes calculating the viscosity at that region really challenging. One way for calculating the viscosity behavior is through displacements. For the glass-forming liquids, the relative displacements become more significant at temperatures greater than T_g , indicating the high deformability of the glassy alloy in the super-cooled liquid region. The self-diffusion coefficient, D, can be calculated by the integration of the velocity auto-correlation function. In this study, we determine D using the linear slope at long times of the mean-square displacement [46, 80]. For this purpose, we used the same simulations that represented in figure 4.4 and we calculated the mean displacement of each type of atom separately during this process. These calculations for AMZ4 while quenching and holding at $T_g + 50$ is represented in figure 4.6. The figures indicated that we need a long offset time to assure the structure is relaxed.

The displacement calculations enabled us to determine the viscosity-temperature relationship. As previously discussed, the slope of the logarithm of the viscosity with respect to the inverse temperature is defined as the fragility parameter; and a strong liquid exhibits an Arrhenius type temperature dependency of the viscosity, whereas the temperature dependence of the viscosity for a fragile liquid deviates from the Arrhenius behavior with a sudden change in the viscosity value around the glass transition temperature. According to Stokes-Einstein equation:

$$D = \frac{k_B T}{6\pi r \eta} \tag{4.8}$$

According to the equation 4.8, the temperature dependencies of $\log \eta$ and $\log \frac{T}{D}$ should be identical. Based on this, we determined the viscosity-temperature relationships of liquids around glass transition. In figure 4.14, the temperature dependency of average viscosity over the cooling rates of the liquid alloys is represented against the reciprocal temperature. The comparison of this relationship to Angell's definition of fragility is revealing the fragile behaviour of Pt-based alloys. Although the range of changes is not consistent with Angell's plot (this is because we indicated the viscosity-temperature relationship through the diffusion coefficient rather than measuring the viscosity itself), the curvature of the plots of Pt42 and Pt60 is exhibiting more changes of viscosity while approaching the glass transition temperature, whereas this behaviour in AMZ4 is following a more linear trend. This is closely related to the dynamic behaviour and kinetics of the spheres in packing configurations, supporting the concept of fragility.

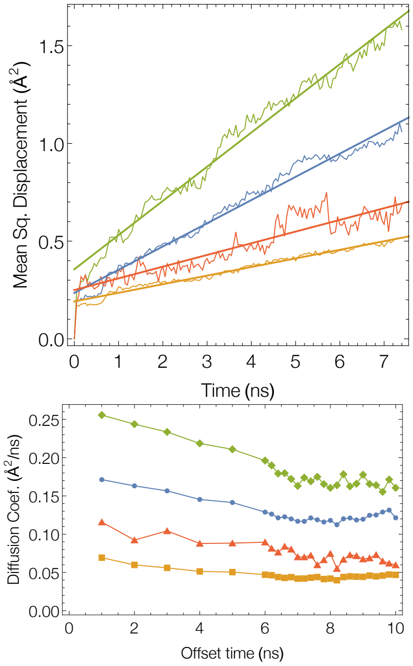

Figure 4.13: Mean Displacement of each atom specie (for the last 7 ns) and corresponding diffusion coefficient calculated for AMZ4 while relaxing at T_g+50 K (here offset means the displacement for that last configuration was calculated for how much time from the beginning of the relaxation.

In the next step, for quantitative comparison of fragility in our metallic liquids, first we calculated the kinetic fragility (m_k), based on the slope of viscosity-temperature curvature around T_g, (the details of these calculations were discussed in the beginning of this chapter) and in another attempt, we determined this parameter by structural definition of fragility. In this study, the structural fragility is determined by a linear fit of the peak position changes data in range $\frac{T_g}{T} = 0.85$ to 1, which is defined by:

$$m_{str}^{r1} = \frac{d(\frac{\Delta r_1(T)}{r_1(T_g)})}{d(\frac{T_g}{T})}\Big|_{T=T_g} \tag{4.9}$$

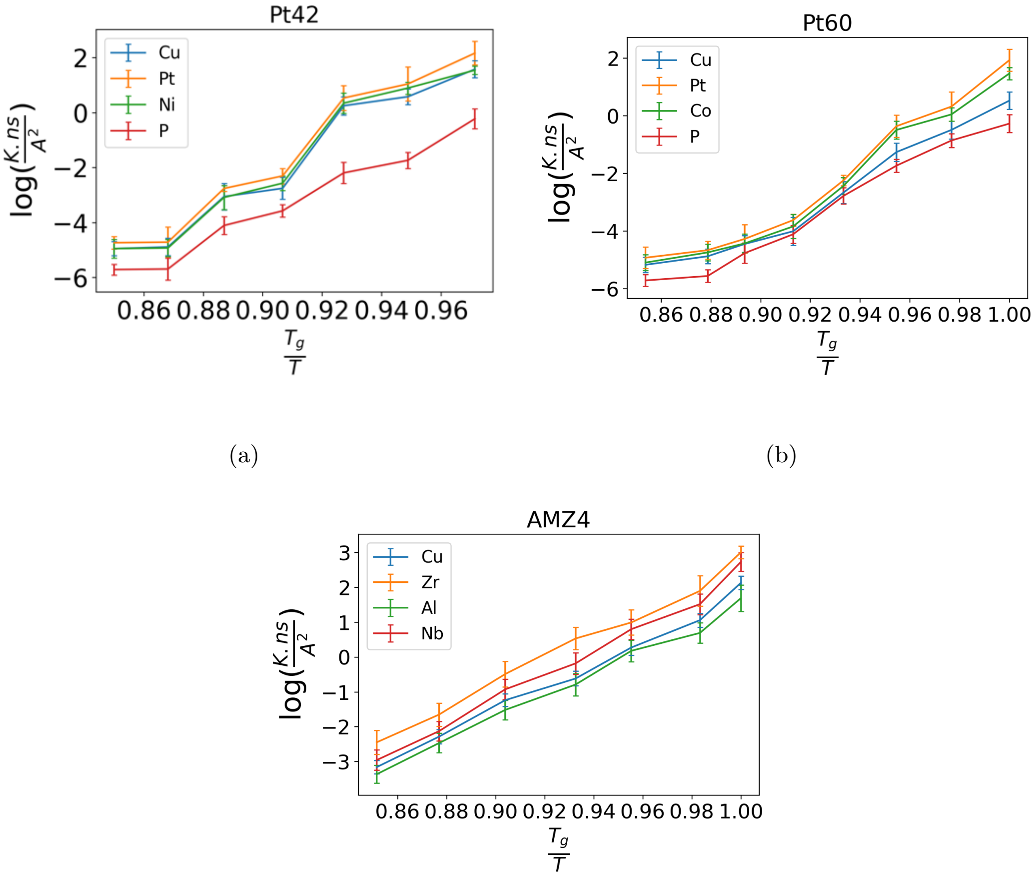

(a)

(b)

(c)

Figure 4.14: Viscosity-temperature relationship of (a) Pt42 (fragile liquid), (b) Pt60 (fragile liquid) and (c) AMZ4 (strong liquid).

The structural definition of fragility can also be determined by the spherical volume shells (rather than changes in the peak positions). First we define the volume changed, followed by volume dilatation as:

$$V_{i-j} = V_i - V_j = \frac{4}{3}\pi(r_i^3 - r_j^3) \tag{4.10}$$

$$\epsilon_{i-j} = -\Delta V_{i-j}(T)/V_{i-j}(T_g) \tag{4.11}$$

where $j = 0, 1, 2, 3$ $(r_0 = 0)$ and $i = j + 1$. This volume dilatation can provide insight on the thermally-induced spacing of spheres. Additionally, structural fragility based on the volume dilatation is defined as:

$$m_{str}^{V_{i-j}} = \frac{d(\epsilon_{i-j})}{d(\frac{T_g}{T})}\Big|_{T=T_g} \tag{4.12}$$

We determined this parameter for the changes from 3^{rd} to 4^{th} volume shell to investigate the correlations with the kinetic fragility. The results of calculated fragility parameters are reported in table 4.6.

Firstly, the kinetic and structural fragility for both of the fragile Pt-based liquids is substantially higher than the ones in strong liquid of AMZ4. Secondly, the relationship

	AMZ4	Pt42	Pt60
m_k	35.61±1.07	44.79±1.21	46.91±1.26
$1/m_{str}^{r1}$	372.67±41.3	1489.1±43.52	1565.35±48.21
$m_{str}^{V^{4-3}}$	0.041±0.05	0.49±0.06	0.46±0.07

Table 4.2: The structural and kinetic fragility of AMZ4, Pt42 and Pt60.

between the kinetic and structural fragility of each glass-forming liquid is demonstrated in figure 4.15. This suggests that there is a linear correlation between these two metrics of fragility, as the greater value of these parameters denotes to the more fragile liquids. This trend is perfect in the structural fragility of the first peak. Structural fragility coming from the 4^{th} volume dilatation still shows the same trend, although it is not capable of distinguishing the fragility quantity of Pt42 and Pt60 properly.

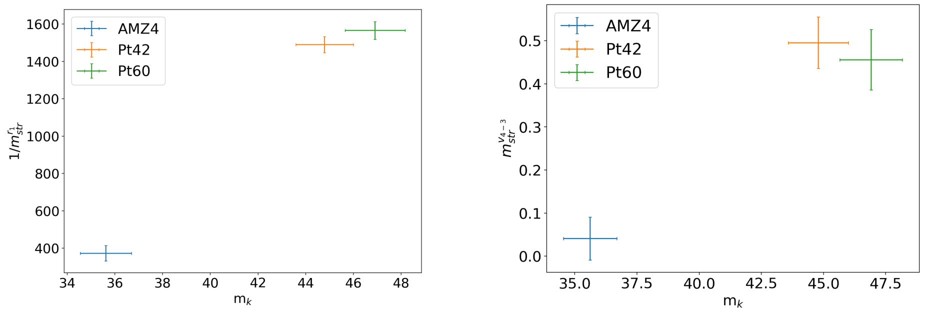

(a)

(b)

Figure 4.15: The relationship between the kinetic fragility m_k and structural fragility m_{str} from the (a) first peak changes and (b) fourth shell volume changes of the PDFs.

We revisit the main question we tried to answer in this chapter: is atomic-size mismatch sufficient condition to yield fragility in bulk metallic glass forming liquid? Possibly! We found that there is a lot of uncertainty in which the peak positions are changing. The peak positions depend on thermal expansion, and also atomic distances. A lot of changes are not coming from the structural change in PDF peak positions, it might just be the ways that we are averaging over the distances.

Moreover, measuring viscosity for these systems over a wide range of viscosities around the glass transition temperature is challenging, and we looked at the entropy approach, but entropy also scales more with the packing density than anything else.

The other insight is that, when liquid is fragile, the structure of the liquid is going to change a lot by changing the temperature, and if we have different sizes of atoms, we have different ways of arranging the atoms packed together. Thus, these degrees of freedom allow to have different structures. The binomial distribution of voronoi volume has also confirmed that they have different structures.

Chapter 5

Identifying Defects in Amorphous Structures

The main objective of this study is identifying the “defects” in amorphous materials — structures with local properties that are outliers in the property distribution and so represent sites of weakness. In this chapter, several approaches are presented for quantifying local structure, and new computational methods are put forward to explain the numerical values of some common amorphous configurations and their characteristics. These models help us to achieve a deeper understanding of the relationship between their structure and properties, and pave the way for the development of a theory of defects in amorphous structures.

5.1 Introduction

Amorphous materials have disordered atomic nature and due to lack of periodicity and any reference structures or equivalent intrinsic entities to compare the amorphous structures with, identifying the defects is more challenging in these structures. Moreover, the positions of atoms in these materials cannot be predicted by any form of equations. However, this does not necessarily mean that amorphous structures are defect-free. As opposed to crystalline structures, where various kinds of defects can be identified, the defects in amorphous structures are still under studied. In crystalline solids, defects are identified as local deviations from the crystal order, whereas it is not clear how defects can be defined in amorphous solids. There is no ideal reference structure and even there is no determination about the size of the region of defect.

Several studies have attempted to identify the defects in the amorphous state and their corresponding effects on mechanical properties of amorphous materials. For example, Christopher A. Schuh et al. [81] have explained the basis of physically sound deformation mechanisms and their contribution to mechanical properties of metallic glasses by focusing on structural evolution in shear bands and strain localization. Egami et al [82, 83] have defined the structural defects in metallic amorphous materials based on the density of atoms and the distribution of the internal stresses on the atomic level in local environments and they explained how amorphous alloys exhibit a scale-dependent distribution of elastic constants. In another study by Keisuke Ide [84], the focus of defects identification in amorphous structure is on electronic defects rather than the structural defects, which may cause instability issues in semi-conductors as they might carry traps in gate insulators, interfaces, and channel materials. In another attempt, Moshe et al [85] have characterized defects in amorphous materials by deviations of the material's intrinsic metric from a Euclidean metric in 2D dimension.

Some of these methods purely depend on geometrical concepts which may vary significantly from one atom to the other and in some other studies, the effect of different types of atoms and other features have not been taken into consideration. In most of these studies, researchers tried to think ahead of time what the defect is and this may put bias in the way they are defining these defects. In an attempt for expanding these theories and automate them, we have developed two predictive models by using machine learning techniques to characterize the outliers in amorphous materials. Over the past few years, machine learning techniques have been used to address the structure-property relations in glasses. Among these studies, Tian et al [86], Cubuk et al [87] and Deringe [88] have achieved broader impact of machine learning in the field of amorphous materials. However, these successes achieved by using machine learning methods are still modest, and do not show sufficiently high accuracy in predicting the site of weaknesses and outliers in amorphous materials. In our study, we implement machine learning methods that are particularly suited for establishing relations where simple theory has previously been intractable. Our models leverage the quantitative attributes for capturing the distinct differences in materials and correlating them with the material's physical and mechanical properties. For this purpose, we use two different models which are discussed in details in the next sections.

5.2 Method 1 - Unsupervised Learning

In the first method, we attempted to use cluster analysis (unsupervised learning) for the purpose of finding similarities between the localized environments in amorphous materials. To begin with, we need a description of the local sites that allows the local outliers' characteristics to be learned. Therefore, we leverage the features that highlight the spatial arrangements and orientation of atoms and their distribution around each other. Here we explain the essential properties that an ideal descriptor may have for encoding the materials. These properties are including:

- Global uniqueness: the mapping of the descriptor should be unique for a given input atomic environment.

- Invariant: meaning that the descriptors should be invariant under symmetry operations—permutation of atoms, rotation and translation of structure.

- Sensitivity (local stability): small changes in the atomic positions should result in proportional changes in the descriptor, and vice versa.

- Dimensionality: the dimension of the spanned hyper-dimensional space of the descriptor should be sufficient to ensure uniqueness, but not larger.

- Interpretability: features of the encoding can be mapped directly to structural or material properties for easy interpretation of the results.

- Scalability: descriptors should be easily generalized to any system or structure with a preference to have no limitations on number of elements, atoms, or properties.
- Complexity: to have a low computational cost, the descriptor should be fast enough to scale to the required size of the simulations and also to be used in high-throughput screening of bigger systems.
- Discrete mapping: the descriptors should always map to the same hyper-dimensional space with constant size feature sets, regardless of the input.

Atomic Environmental Vector:

Based on the ideal properties of a descriptor, local representations of the atomic environment can be highlighted by a metric called Atomic Environmental Vector (AEV) [89, 90]. Basically, AEV is a vector that can represent the local environment of each atom properly by combining a radial and angular term in a one dimensional vector. The radial symmetric functions of AEV is defined as:

$$G^{R}_{i;\alpha,m} = \sum_{j\neq i, j\in\alpha} e^{-\eta_R (R_{ij}-R_s)^2} f_c(R_{ij}) \tag{5.1}$$

where α and β in radial and angular terms are the elements of the neighbours within a cutoff radius R_c and index m here runs over the set of parameters $\{\{R_s\},\{\eta_R\}\}$ and the summation j runs over all the atoms of element α; here η_R controls the width of the radial Gaussian distributions, and R_s controls their radial shift. Also $f_c(R_{ij})$ is the cutoff function which ensures the locality and is defined by:

$$f_c(R_{ij}) = \begin{cases} \frac{1}{2}(cos(\frac{\pi R_{ij}}{R_c}) + 1) & R_c \geq R_{ij} \\ \\ 0 & R_c < R_{ij} \end{cases} \tag{5.2}$$

And the angular symmetric function is defined by:

$$G^A_{i;\alpha,\beta,n} = 2^{1-\zeta} \sum_{j,k \neq i} (1 + cos(\theta_{ijk} - \theta_s))^{\zeta} e^{\eta_A (\frac{R_{ij}+R_{ik}}{2} - R_s)^2} f_c(R_{ij}) f_c(R_{ik}) \tag{5.3}$$

where the index n runs over the set of parameters $\{\{R_s\}\{\theta_s\}\{\eta_A\}\{\zeta\}\}$ and the summation runs over pairs of atoms of elements α and β. Here again η_A and R_s have the same role as in the radial symmetry function described above, with θ_s capturing different regions of the angular environment and ζ controls the width of the peaks in the angular environment. For the angular function, the spatial weight is implemented which compensates for the more atoms which are falling into the central circle as it is bigger than the other circles further away (shown in figure 5.1). Additionally for the radial function, the radial weight is used to highlight the importance of the bonds with neighbours closer to the central atom (first shell) comparing to the atoms which are further away (second, third,.. shell). This is exhibited in figure 5.1:

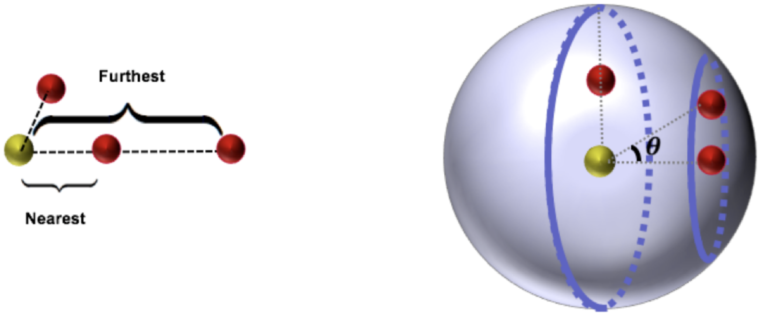

Figure 5.1: AEV radial (left) and spatial (right) scales.

In this method of defect identification, several snapshots of amorphous metallic glass of AMZ4 were used for AEV analysis. We started the simulation by holding AMZ4 for 3 ns at 1600K and then cooled the structure down to 50K, 150K and 450K above the glass transition temperature of AMZ4 (the glass transition temperature calculation was previously discussed in section 4.3.2.). Then the system was held for another 7 ns at these temperatures to ensure the equilibrium. In the next step, we calculated the AEV vector for the different snapshots of this metallic amorphous liquid. We use AEV for each atom type (Cu, Zr, Al and Nb) to identify classes of environment experienced by each element. In figure 5.2, the radial and spatial term of AMZ4 has been represented. We have put some constraints on θ_s and R_s to make sure the computations are efficient and AEV vectors are not too large.

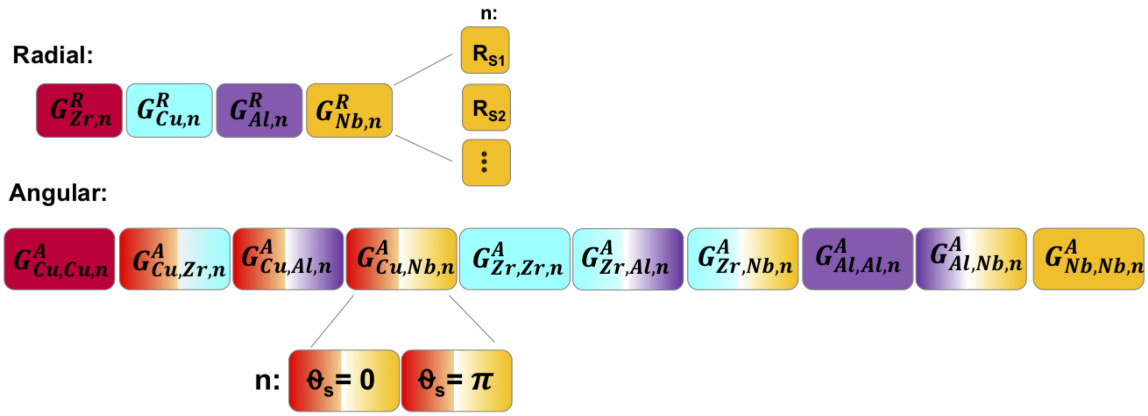

Figure 5.2: Radial and spatial terms of AEV in AMZ4.

These local representations of the atomic environment have high dimensions which adds complexity and noises to our model. For this reason, we have implemented Principal Component Analysis (PCA) [91] to simplify the complexity of our high-dimensional data while retaining the trends and patterns. PCA is an established method of reducing dimensionality to a subset of important features, which holds the same descriptive information of the local structures. The benefit of using PCA is that we do not lose information and at the same time, PCA removes any high correlation between the local representations which may induce bias while learning the data.

We chose the few first significant components and these components were sufficient to extract the dominant patterns within the AEV (The first three components are shown in figure 5.3).

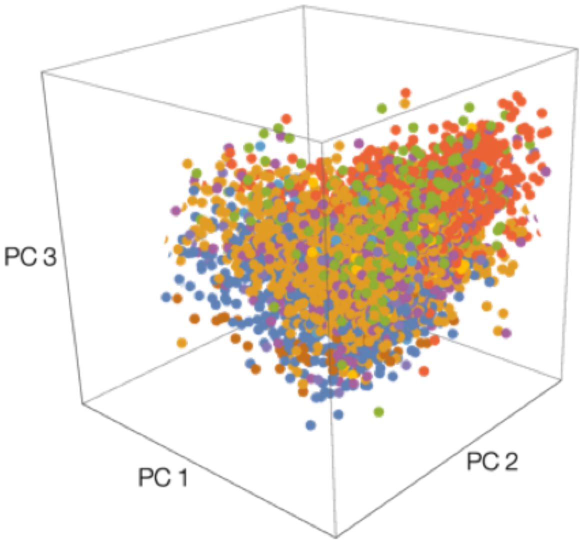

Figure 5.3: Three principle components from AEV.

After normalizing the AEV and performing PCA, the next step is feeding the components of each species as an input to our unsupervised model. For cluster analysis, we implemented Gaussian mixture model [92] which is a probabilistic model that assumes all the data points are generated from a mixture of finite number of Gaussian distributions and each of these distributions represent a cluster. For these models, we specifically used scikit-learn library in Python [93]. The main reason for choosing this algorithm among the other clustering methods is that, when observing the PCA, the data sets represent normally distributed sub-populations and suggest that the local identifiers in our data set comes from a Gaussian distribution with a different mean and variance.

5.2.1 Results

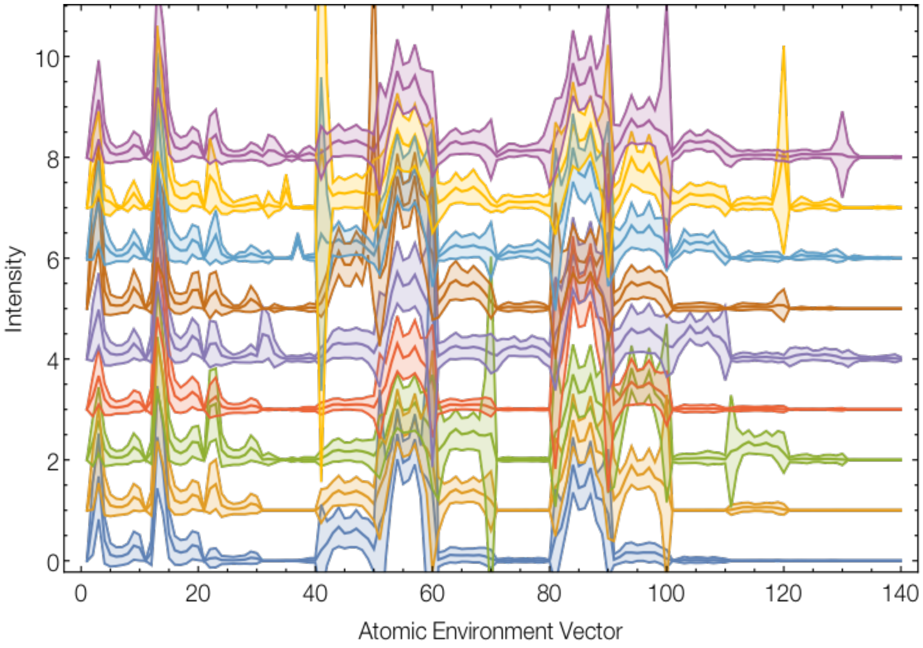

Figure 5.4: Average AEV of different clusters for Cu in AMZ4

In figure 5.4, the average AEV of each cluster (in total of 9 clusters) after cluster analysis is represented. Each color in the figure denotes to one cluster and the band with 3 lines of plots for each cluster represent the mean AEV (the middle one) and one standard deviation below and above the mean AEV. For each cluster, the intensity of radial distribution of the average AEV remains almost the same (in the AEV range of 0 to 20 in figure 5.4). However, the elements that differentiate these average AEVs (clusters) from each other is mostly the angular term of AEVs. For example, in the first two AEVs (purple and yellow ones), there is a wide range of intensities, which are causing the sharp peaks at the tails of the plots. When we have intensity of zero, means that there is no triples of three types packed together, and when there is a peak at the tail, this means that there are a lot of triples that made the angles all over the system. Therefore, rather than focusing on the angles and how they are different between triples of atoms, this method focuses on the existence of these angles. This means that PCAs were grouped by the chemical environments rather than the structural environment, which makes this model not effective enough to distinguish the structural environment experienced by each atom. To investigate more, cluster analysis for each type of atom in AMZ4 was performed.

The result of this analysis for three different temperatures that previously mentioned has been shown in figure 5.5. Base on this figure, we can identify outliers in 3 possible ways: (i) structures with AEV distant from the exemplars of all the other clusters (ii) AEV clusters with only a small number of members (iii) AEV structures common at high T but rare at low T. The local structures which are far from the other clusters are AEV cluster of 2 in Cu, 5 in Zr and 2 in Al which has much higher frequencies than the others and the AEV clusters with smaller number of members are 6,7,8 in Cu 6,8 in Zr and 5 in Al. Geometrically, the smaller member AEV clusters corresponds to rare spatial orientations of atoms that have the properties of outliers after PCA projection. On the other hand, the third way which takes the thermal excitements into account, attempts to identify the defects based on the magnitude of frequency fluctuations in each of the clusters. By this definition, we can observe that in the Cu case, the difference of cluster 2 and 4 for each temperature is more significant than any other AEV cluster, thus AEV cluster of 2 belongs to outliers induced by thermal excitements.

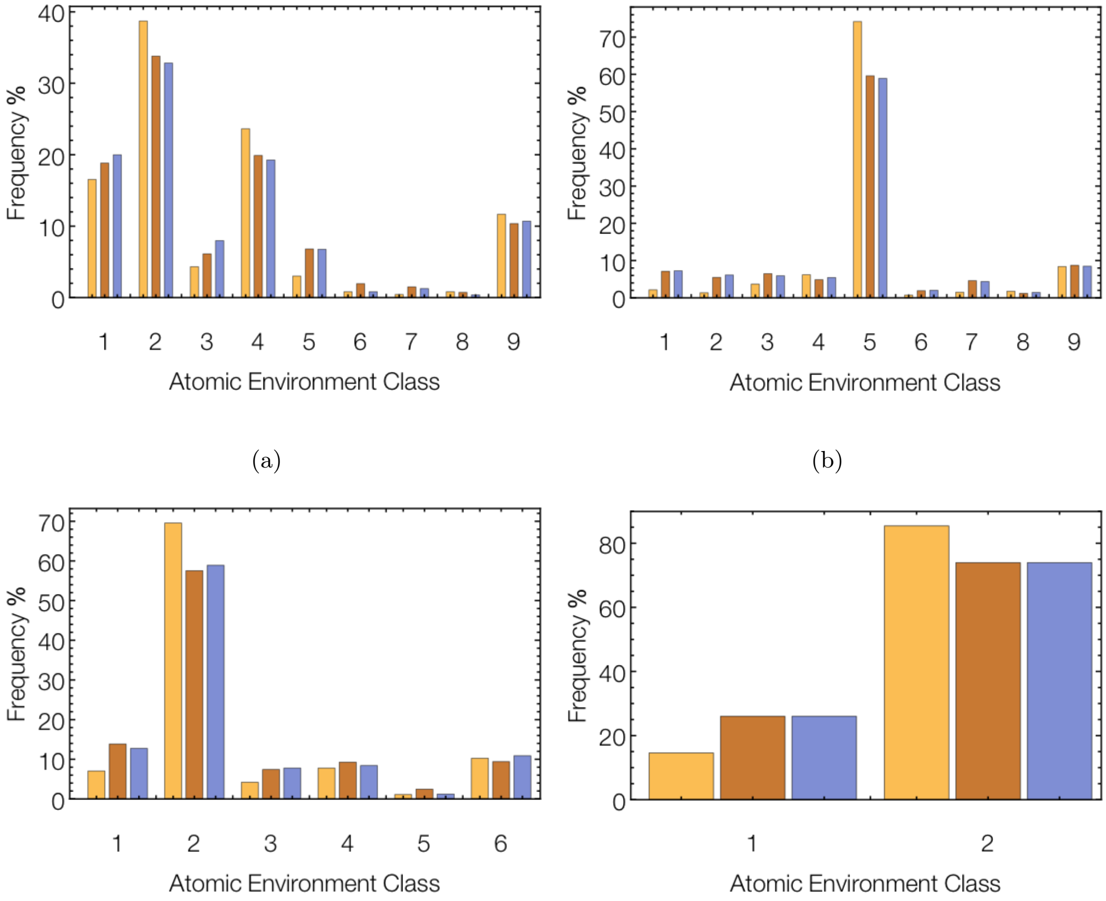

(a)

(b)

(c)

(d)

Figure 5.5: Classes of defects detected by AEV: (a) classes of Cu (b) classes of Zr (c) classes of Al (d) classes of Nb

As previously discussed, cluster analysis can provide a guidance on possible defects identification in amorphous structures; however, it still suffers from the clear and powerful description of defects as there are multiple possible ways to categorize the outliers and linking these clusters to the properties of the material is still challenging. Additionally, cluster analysis methods may overestimate the similarity between environmental groups and do not treat local structures as individuals. For this reason, we propose an alternative powerful method to identify the local outliers that address the challenges of the previous model. This will be discussed in details in the next section.

5.3 Method 2 - Weak Supervised Learning

In our second model, a new machine learning technique is put forward to describe and define the localized defects in amorphous materials, in particular, metallic glasses, which also contributes to a better understanding of atomic arrangements in these amorphous solids. In order to build this predictive model for identifying defects, we leverage the features which highlight the spatial arrangements and orientation of atoms, their distribution and local characteristics. These parameters explore the symmetric and atomic environment as well as relevant descriptors quantifying the structure surrounding each particle. The performance of this algorithm is then characterized on other glasses.

This method, particularly involves statistical analysis of a novel model to investigate the probability of defects in glasses and to obtain their contributions to the properties of the material. The most challenging part is how to label the defects in these materials as there is no predefined defects, like the ones in crystalline structures, to train and build our predictive model based on those. At the same time, there are some heuristics that can guide this identification. These heuristics are based on the other experimental and theoretical studies on the amorphous structures, and they enhance the logic behind our model.For this purpose, both generative and discriminative models were performed using Snorkel library in Python, developed by Stanford researchers [35]. Weak supervision learning provides us signals for labeling the large amount of data in order to create a powerful predictive model. This algorithm generates higher-level supervision in the form of labeling functions (heuristics) that capture our domain knowledge and resources, without having to carefully manage the noise and conflicts inherent in combining labeling functions. Since labeling functions are self-contained and operate on discrete local environment, their execution is parallel and we can observe the coverage, correlations and overlaps between labels provided by these labeling functions. Weak supervised learning maps the attributes in the representation of the physical properties to more accurate definition of defects.

5.3.1 Features

To begin with, we used the same amorphous metallic glass (as previous chapter) of Pt42 with 7528 atoms. After holding this system at 1200 K (which is above its glass transition temperature) for 7 ns, we cooled the system down to 0 K with different cooling rates of 1.2, 0.6, 0.4 and 0.24 Kps^{-1}. For each system, we have built the labeling functions based on the local environment of each atomic species in our glass models. One of the features, SOAP, relies on a Gaussian smeared atomic density based on spherical harmonics and radial basis function. The other feature that has been used is Atom-Centered Symmetry

Functions (ACSFs) which represents the configuration of atoms around a single central atom using symmetric functions. LMBTR was also calculated for encoding the local structures by using a distribution of different structural motifs and kernel density estimation which is constructed based on the distribution of atoms. These features were all created by DScribe library [51] in Python, which transform atomic environment into numerical features. More details on each of these descriptors were discussed in chapter 3.

The descriptor of SOAP within the cutoff of 6 $\AA$ around each atom of Pt42 with cooling rate of 1.2 Kps^{-1} has been shown in figure 5.6. The SOAP figure indicates that there are some signals at certain distance far from each atom, and at the same time not all the elements of SOAP can provide us useful information (where SOAP intensity is 0). Therefore, our focus is only on the main signals of SOAP.

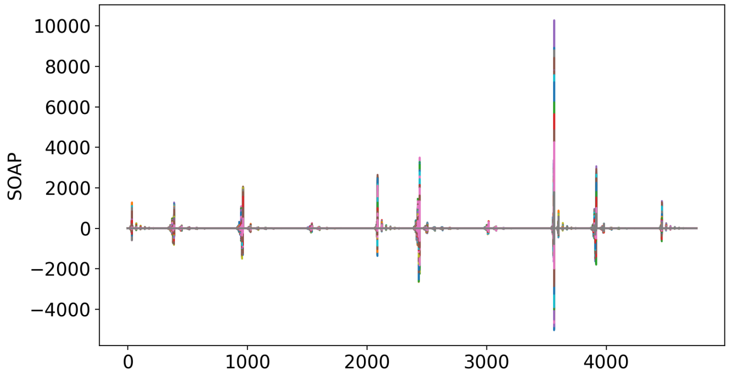

Figure 5.6: SOAP vectors for all 7528 atoms in Pt42.

Apart from SOAP, LMBTR is another feature that we implemented in our labeling functions. LMBTR for the same system of Pt42 is also represented in figure 5.7. For this calculation, exponential weighting function was used which controls the atomic density; basically, atomic density function decays to the threshold of $1e^{-3}$. The differences in the local environments also hints at the intense signals of LMBTR.

The last feature that we implemented for our generative model is ACSF with the same cutoff of 6 $\mathring{A}$ which is shown in figure 5.7. We specifically used heat-map for visualizing and getting a better idea of the ACSF ranges across local environments. In ACSF calculations, the central element is not taken into consideration, and it solely highlights the arrangement of neighbours. We observed that in the first shells and nearest neighbours, ACSF is relatively small. This was also seen in distances further away from the local environments. However, in intermediate-range order, the ACSF exceeds the value of 10, where the symmetry of the neighbouring atoms is more pronounced.

5.3.2 Labeling Functions

The next step after creating the features is building the labeling functions. For this purpose, we used inter-quartile ranges [94] for the descriptors which is a common method to detect the outliers in the data sets. The thresholds based on inter-quartile method are defined as:

$$IQR = Q3 - Q1 \begin{cases} LowerBound : (Q_1 - 1.5 * IQR) \\ \\ UpperBound : (Q_3 + 1.5 * IQR) \end{cases} \tag{5.4}$$

where IQR denotes the inter-quartile, Q_1 is the first quartile of the data, meaning that 25% of the data lies between the minimum and Q_1, and Q_3 is the third quartile of the data, meaning that 75% of the data lies between the minimum and Q_3. Lower bound and upper bound have been defined as our measure of outlier detection, meaning that if the local environment of any descriptor, falls above the upper bound or below the lower bound, we identify that structure as an outlier and we label it defective in our labeling function. Also we use the same idea to label the data non-defective if the local environment's feature is falling on the average of each of these descriptors.

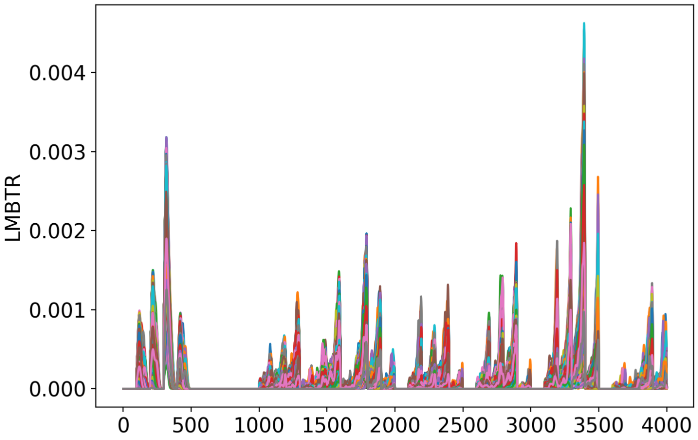

Figure 5.7: LMBTR vectors for all 7528 atoms in Pt42.

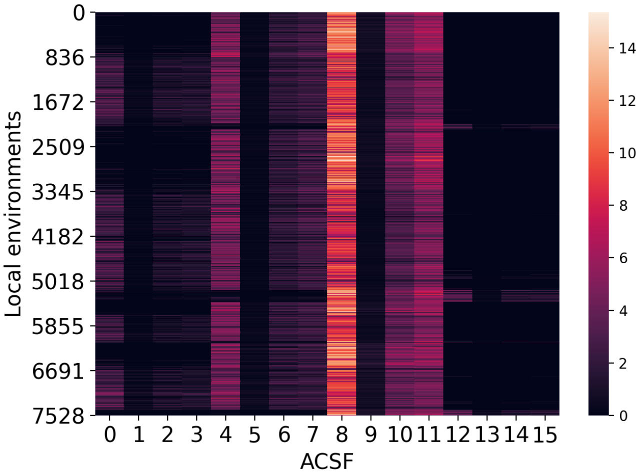

Figure 5.8: ACSF heat-map across all the local environments of Pt42.

After creating the labels, the generative model was trained via the labeling functions, and the output was the probability of each local environment being defective. These probabilities were further used as the input of the discriminitive model, for which the artificial Neural Network [95, 96] was implemented.

Neural Networks (NNs) are inspired by sophisticated functionality of human brains where hundreds of billions of interconnected neurons process information in parallel. The NN that we implemented is comprised of an input layer, one hidden layer and the output layer. The input to a given node of the hidden layer is a weighted sum of all the descriptors in the input layer (the logic behind our NN is shown in figure 5.9). By this NN, we trained a powerful predictive classification model using the labels we created by generative model; the model basically outputs the probability of a local environment being defective by using descriptors of each local environments. These probabilities were then converted to binary classes, by using the threshold of 0.5, meaning that any local structure with the probability of higher than 0.5 would fall into the defective environment.

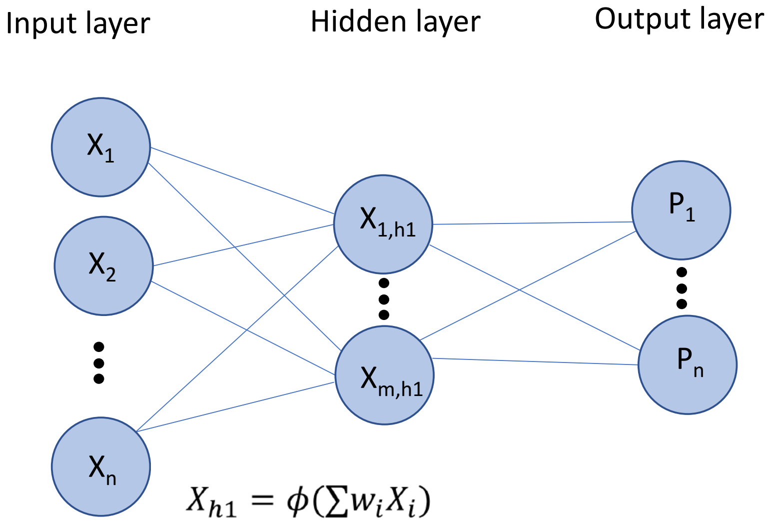

Figure 5.9: Neural Network model used as our discriminative model, which is comprised of an input layer, one hidden layer and an output layer.

5.3.3 Results

The trained discriminative model was implemented to identify and investigate the defective environment. Identifying the defects was followed by structural characterization to shed light on the correlations between various packing configurations and the identified outliers. For this purpose, first we visualized the distribution of the identified outliers in the system. The defective environments were distributed all over the system and we did not observe any sign of segregation.

In the next step, the relative centroids of voronoi volume and the local structures were determined. The relative centroid is the distance between the center of the atom and the center of the polyhedral cell that the atom is trapped in. These centroids were then normalized by the radius of each species to disregard the different spacing caused by the sphere size. The radius for each atom type in our model was calculated by the pair distribution function between each pair of the same atomic species. The first peak of the pair distribution function for Cu-Cu, Pt-Pt, P-P and Ni-Ni pair atoms were separately calculated and as the first peak exhibits the distance between the centroid of each atom to its nearest neighbor atom, we can achieve the radius of these four element types.

In figure 5.10, the distribution of these normalized centroids for different species of atoms as well as the identified defects (red bars) is shown. Surprisingly, the red bars belonging to defects indicates the larger distance between the center of the local defects and their corresponding polyhedrons, meaning that the distribution of the relative centroids for identified defects does not follow the distribution of all the local environments. Larger relative distance of centroids also occurs in vacancy defects in crystalline structures, where an atom is missing in the neighbour of a sphere and causing the centroid of the surrounded polyhedron fall further away from the centroid of the atom.

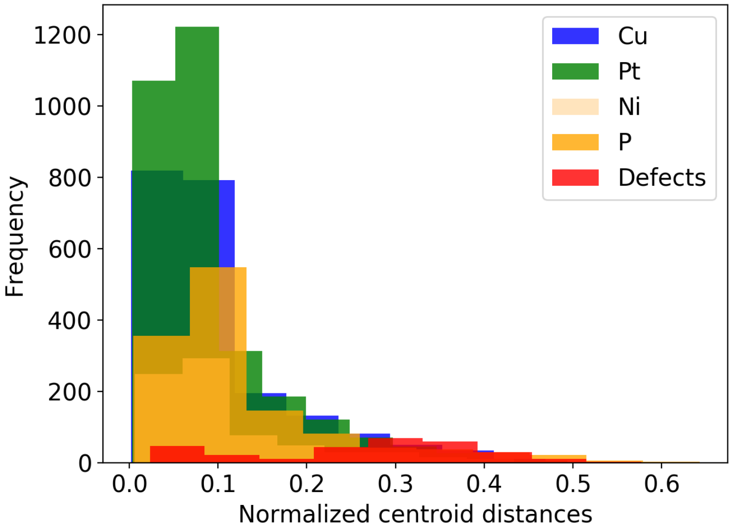

Figure 5.10: The distribution of the centroid distances normalized by sphere sizes.

Supporting this idea, we looked into the random sample of defective and non-defect environment's polyhedrons (this is represented in figure 5.11). These polyhedrons suggest that regardless of the atomic type, the more distorted polyhedrons belong to the defects. The defective polyhedrons mostly have several planes which are significantly larger that the other planes of the polyhedral cell. As discussed, this confirms the similar concept of having vacancies like the ones in crystalline structures. It also has connection with the larger free volumes that previously observed in voronoi volume distribution.

To investigate the connection between the identified defects and the amorphous material's properties, we set up a simulation. We performed this simulation on our system of Pt42 to gain more information about how the defects were identified by weak supervision model. For this simulation, we deformed the system with engineering strain rate of 3% in xy direction using the nve ensemble, and then we observed any events caused by the applied strain. At the same time, we recorded the voronoi volume, potential energy and the stress on each of the local environments while the deformation was being applied.

(a)Perfect Cu (b)Defective Cu

(c)Perfect Pt (d)Defective Pt

(e)Perfect Ni (f)Defective Ni

(g)Perfect P (h)Defective P

Figure 5.11: Sample of perfect polyhedrons and defective polyhedrons of each species. Regardless of atomic species, the defective polyhedrons are more distorted comparing to non-defective polyhedrons.

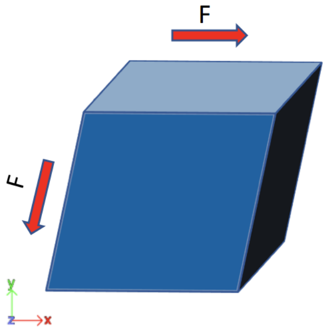

Figure 5.12: Shear strain deformation in xy direction of a block of Pt42 to investigate the events related to the defective environments.

In figure 5.13, the left figure represents the average potential energy change for all the atoms (blue line), where plasticity occurs after 1.5 % strain. The red line belongs to the average potential energy change of defective environments. The green line is the average potential energy change for a random sample of non-defective environments with the same number of samplers as the defective environments. Although the average potential is going up, average potential of the defects is decreasing around where the sign of plasticity appeared. The defective structures have significantly deviated from the average potential energy. This suggests that during plasticity, these defective environments first have minimized their potential as opposed to behaviour of the non-defective environments, as they overcome the saddle points during this process. The random sample is also around the average potential of all the defects and indicated the variation of potential energies that we may expect around the average energy change.

Figure 5.13.b represents the minimum potential energy change for the same environments. The lowest potential energy within all the defective structures (red line) has

the largest negative potential change in the entire group (in around 0.7% strain), meaning that largest jump of energy in the whole system belongs to the defective structures. This relatively large change is overlapping with the minimum potential of the entire system, meaning that when the deformation happens, the defective environments are contributing to the plasticity of the system.

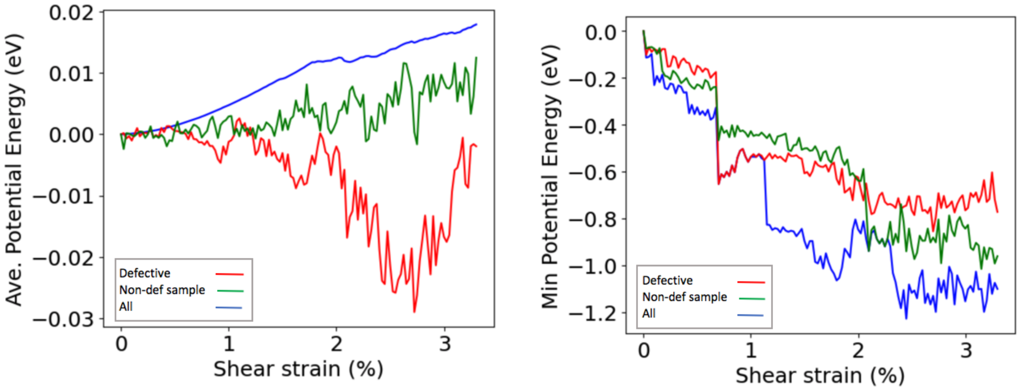

(a) (b)

Figure 5.13: Average potential changes and minimum potential changes while deforming the system.

Figures 5.14 represent the voronoi change for all the local environments recorded for the time steps of applying the shear strain rate. The defects structures are shown by the black lines. The identified defects by our model have mostly increasing trend in their voronoi volume, and because the atomic volume remains the same, this means that the free volume of the defects have an increasing trend under deformation process. However, this

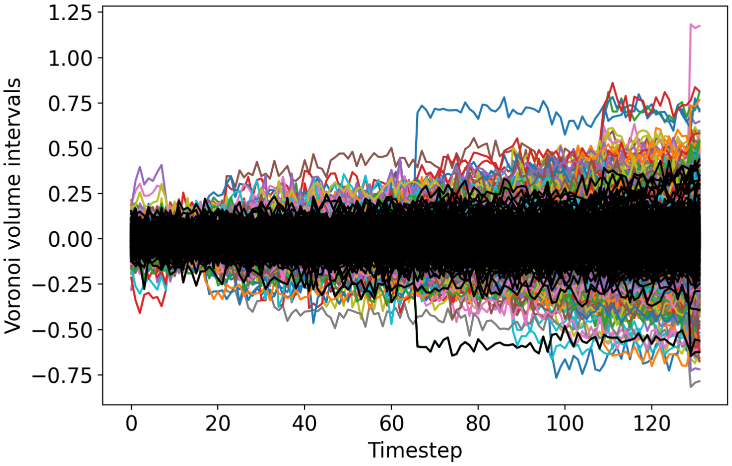

Figure 5.14: Voronoi volume change in each time step of the strain process, the black lines denote to identified defects.

trend is not significant and is not representing the whole structures of the defects and it is still under investigation.

In the final step, we looked into the distribution of the potential energy for all the structures (including defective and non-defective structures) and we compared that to the potential energy distribution of the defects (this has been represented in figure 5.15). There is no obvious trend, and the distribution of defects follows the distribution of the whole system.Additionally, we utilized the same trained model (NN) on different cooling rates of Pt42 to look into the defective probabilities (in figure 5.16). We have only represented the local environments that predicted as defective (having the probability greater than the threshold of 0.5). Even though the rate of the cooling was different for Pt42 systems, the number of defective environments was almost the same (all the structures with defective probability more than 0.5). However, the distribution of these probabilities is different.

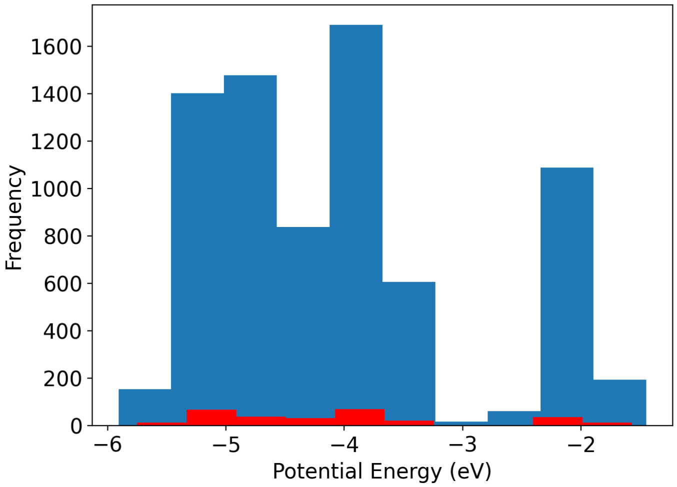

Figure 5.15: Potential energy distribution for all the environments (blue) and for the defective environments (red) in Pt42.

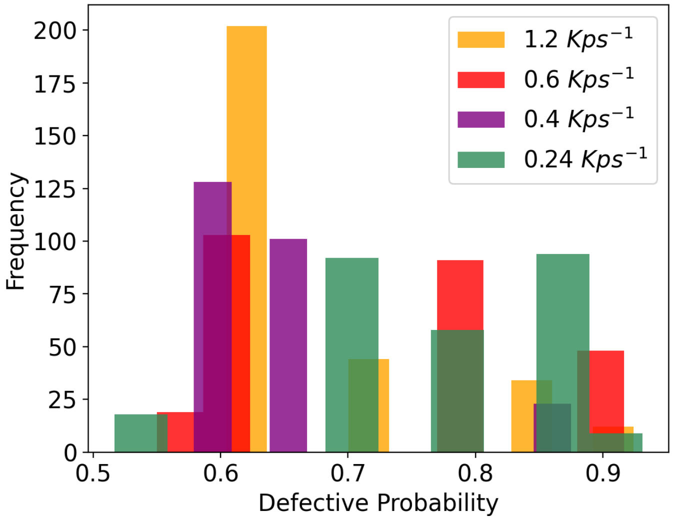

Figure 5.16: Probabilities of being defective for Pt42 local environments obtained by quenching with different cooling rates.

This combined with the previous representation of potential energy distribution indicates that the identified defects by our model are not necessarily frozen in and they are not correlated with energy (as the energy of the defects is distributed everywhere within the all environments' energies and the distribution of the defects is not different from the distribution of all the other atoms). Therefore, these defects are not energetic outliers, as when we changed the cooling rates, we expected to have more high energy defects frozen in, but this was not the case. Therefore, they are rare structures but there is no energy reason why they are rare. These identified defects are associated with the sites of weakness which causes their initial significant jumps when deforming the system.

Chapter 6

Thermal Conductivity in Pristine and Defective LiAlO$_2$

Lithium aluminate (LiAlO$_2$) is an important material as a lattice matching layer for GaAs growth, as a electrode coating and a membrane for molten-carbonate fuel cells, and as an additive in composite electrolytes and in Li-ion batteries. In all of these applications, thermal properties of LiAlO$_2$ plays a key role in their performance.

Lithium aluminate is existing in three allotropic forms of alpha, beta and gamma with hexagonal, monoclinic and tetragonal crystal structures, respectively. In this work, we focus on the tetragonal allotrope of LiAlO$_2$ (gamma-LiAlO$_2$) which has the lattice parameters of a = 5.1687 $\mp$ 0.0005, c = 6.2679 $\mp$ 0.0006 $\AA$. The structure of $\gamma - LiAlO_2$ is shown in figure 6.1.

The metastable β-modification, with a monoclinic structure, transform to the γ-modification at about 900 C. γ-LiAlO$_2$ is an isolator with direct band gap. In this material,

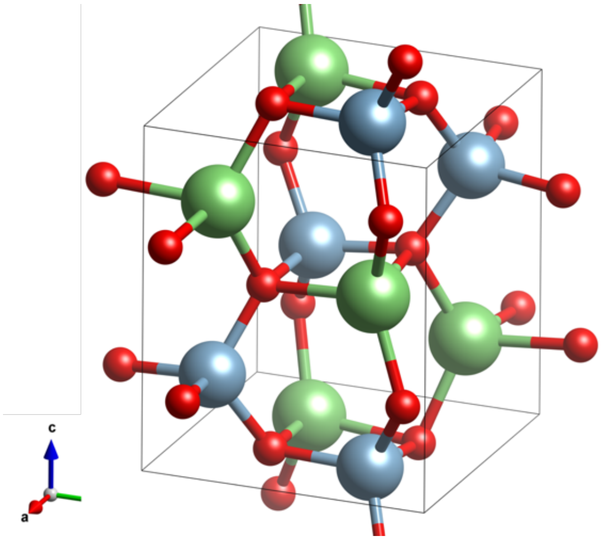

Figure 6.1: Structure of γ-LiAlO$_2$. Red, green and blue atoms belong to Oxygen, Lithium and Aluminum respectively.

the Al-O bonding has covalent characteristic, whereas the Li–O bonding is predominant ionic [97, 98].

In this chapter, we aim to understand the evolution of the thermal conductivity of LiAlO$_2$ and we elucidate the effects of defects on its thermal properties which is important to assure the material's long-term performance and address these effects properly. The defect in LiAlO$_2$ is defined as the localized disruption to the perfect crystalline order. The defects can be in atomistic scale such as vacancies, impurities or displacement and also they can be in sub-grain scale like the dislocation, inclusion and voids. Another scale of defects is grain-scale when the defects is bonded with the grain boundaries and grain misorientation.

In this chapter, classical MD simulations and their results for the purpose of thermal conductivity calculations using the equilibrium Green-Kubo and non-equilibrium Muller Plathe methods are discussed in details (these methods were previously elaborated in chapter 3). Furthermore, the MD simulations were extended to defective structures and we discuss the results from the additional scattering rate due to the presence of these defects in details.

6.1 Thermodynamic Properties Calculation

Thermal conduction is defined as the transport of energy due to random molecular motion across a temperature gradient. Generally, a material's thermal conductivity is the number of Watts conducted per meter thickness of the material, per degree of temperature difference between one side and the other. Thermal conductivity determines the intrinsic ability of a material to transfer or conduct heat and for a specific material, it is highly dependent on a number of factors. This includes the temperature gradient, the properties of the material, and the path length that the heat flows. Also the temperature of a material has a large influence on the thermal conductivity since molecular movement is the basis of thermal conductance. Atoms move more quickly at higher temperatures, and therefore heat will be transferred through the material at a higher rate, meaning that the thermal conductivity of the same material has the potential to change drastically as the temperature increases or decreases [99].

Heat transfer processes can be quantified in terms of appropriate rate equations. The rate equation in heat transfer mode is based on Fourier's law of heat conduction. Fourier's law states that the rate of heat transfer through a material is proportional to the negative gradient in the temperature and to the area, through which the heat flows. The

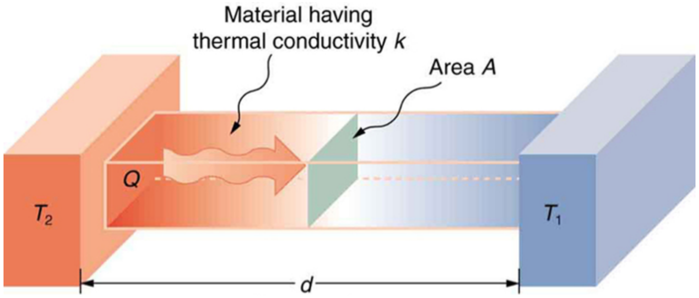

Figure 6.2: Fourier's law of heat transfer

equation for Fourier's law of heat transfer is:

$$\vec{q} = -\kappa \nabla T \tag{6.1}$$

where $\vec{q}$ denotes the local heat flux density, κ is the material's conductivity and ∇T is the temperature gradient. Despite the fact that it is easy to solve this equation for T(x) to find the heat flux, this equation has no connection to the underlying mechanism of heat transport [100].

6.1.1 Pristine $LiAlO_2$

We have tried to compute the thermal conductivity tensor of pristine $LiAlO_2$ using a variety of different methods in order to compare sources of error and to benchmark thermal conductivity calculation methods that use empirical potentials. First, we implemented Green-Kubo (equilibrium method) using LAMMPS package to compute the thermal conductivity from the lifetime or dissipation of fluctuations in the instantaneous heat flux auto-correlation (equation 3.11).

To begin with, we first computed the thermal expansion coefficient and the average lattice parameter of the crystal at the simulation temperature. This was achieved by a MD simulation in the npt ensemble in which the temperature was ramped from 100-750 K. For this simulation, we held the pressure at 0 bar, and while the system was permitted to fluctuate, the system was restricted to remain tetragonal. To obtain the average lattice parameter as a function of temperature, we performed a polynomial fit. Figure 6.3 represented the thermal strain of the discussed ramp.

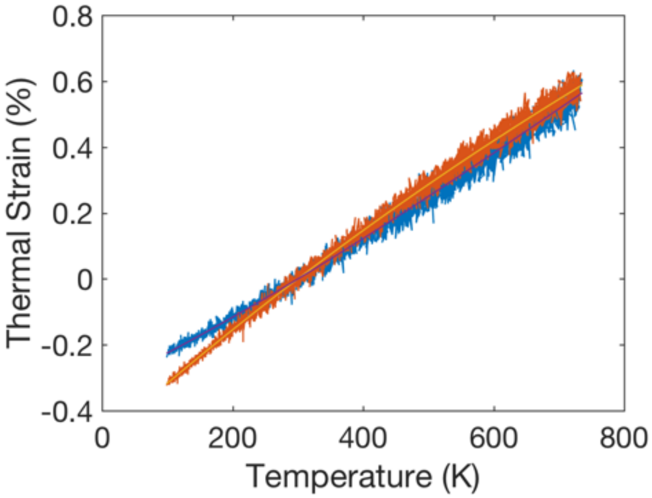

Figure 6.3: Thermal expansion of $LiAlO_2$ in a-axis (blue line) and c-axis (red line).

For calculating the thermal conductivity, the size of the system dictates the number and wavelength of modes available to contribute to the heat current, J, and its dissipation. Therefore, we tested the system size convergence by computing thermal conductivity for systems of increasing size. To keep the simulation box as close to cubic as possible, we selected super-cells with dimensions of 6x6x5, 7x7x6, 8x8x7, 10x10x8, 11x11x9 and 12x12x10.

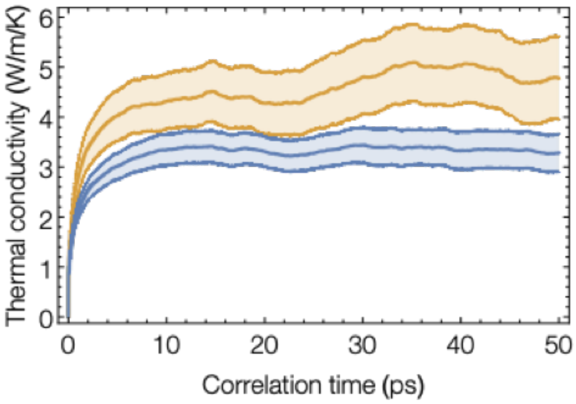

Figure 6.4: Cumulative thermal conductivity vs heat flux correlation time computed using the Green Kubo for a-axis (blue line) and c-axis(gold line).

The correlation function in the equation 3.11 is very slow to converge, and thus to gain a good ergodic sampling, it is necessary to average the correlation functions computed from at least 10 simulations with uncorrelated starting configurations (with each simulation performed over several ns). We have thus performed nve simulations of the correctly scaled systems to generate 10 snapshots of each system with uncorrelated configurations. The final step was to perform the GK simulations [55]. For each snapshot, a simulation was carried out with holding the system for 50 ps in nve ensemble to assure the system lost the memory of the prior nvt simulation, and then the simulation was continued for another 2 ns during which the correlation function was computed. For calculating and integrating the heat current auto-correlation, we first tested the simulation duration and the number of simulations require to average over in, to obtain suitable uncertainty. As mentioned before, we built up 10 different initial configuration and the simulations were carried out for each of them. As it is represented in figure 6.4, the heat flux auto-correlation is highly oscillatory due to the multiple flat optical branches.

Enthalpy correction:

For the better convergence, we attempted to include a multi-component enthalpy correction. For setting up the simulations, the species averaged enthalpy correction to the instantaneous heat flux was computed. As mentioned before, the Green-Kubo method computes the thermal conductivity from the lifetime or dissipation of fluctuations in the instantaneous heat flux. Here we represent the heat flux equation:

$$J = \frac{1}{V} \sum_{i=1}^{N_{at}} ((PE_i + KE_i)v_i + \sigma_i . v_i) \tag{6.2}$$

where V is the volume, PE_i is the potential energy per atom and KE_i is the kinetic energy per atom. v_i and σ_i denote the velocity and stress per atom, respectively [101, 102].

As $LiAlO_2$ is a multi-component system, the center of mass of each species is not conserved, and as the potential energy term (PE) in the flux can have any arbitrary offset for different elements, this can introduce a spurious non-thermal contribution to the energy flux. Based on the equation below for heat flux calculation:

$$J_{cor} = \sum_{\alpha=1}^{N_s} h_\alpha \sum_{i=1}^{N_\alpha} v_i \tag{6.3}$$

where N_s is the number of atom types in the system, h represents the averaged enthalpy per atom of species α and v_i is the velocity per atom i, for enthalpy correction, we subtract the non-thermal contribution to the energy flux off with the correction term given by equation 6.3 based on h, the time and ensemble averaged enthalpy per atom of species alpha. The enthalpy term includes virial and kinetic contributions to the PV term. After implementing the enthalpy correction mentioned above, the MD simulations for Green-Kubo calculations were performed again. The oscillatory auto-correlation is indicated in figure 6.5 .

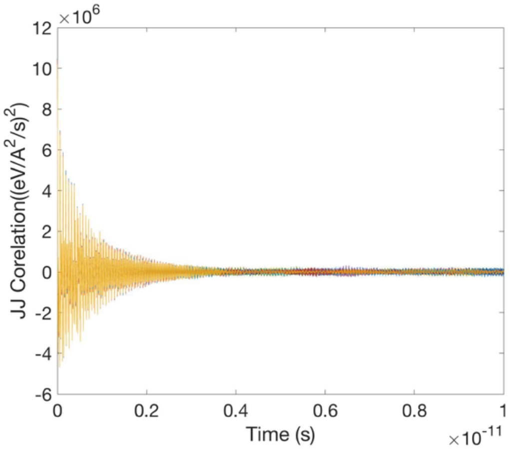

Figure 6.5: Heat flux auto-correlation from MD simulation.

In thermal conductivity calculations for $LiAlO_2$, the simulation is performed with considering the periodic boundary conditions. Periodic boundary condition causes no impediment to phonon movement, meaning that phonons can cross the periodic boundaries; therefore, we can simulate systems that are much smaller than the phonon mean free paths. In these simulations, the system size effect arises as the periodic boundaries limit the largest wavelength of phonons that fit into the simulation box. Additionally, the long wavelength acoustic modes have the longest mean free path, which can lead to an underestimation in thermal conductivity. System size also limits the phonon modes available for anharmonic scattering processes which can lead to an overestimation of thermal conductivity.

After integrating the tail of the auto-correlation function, based on equation 3.11, the thermal conductivity in each direction was calculated and the result for each system size is shown in figure 6.6.

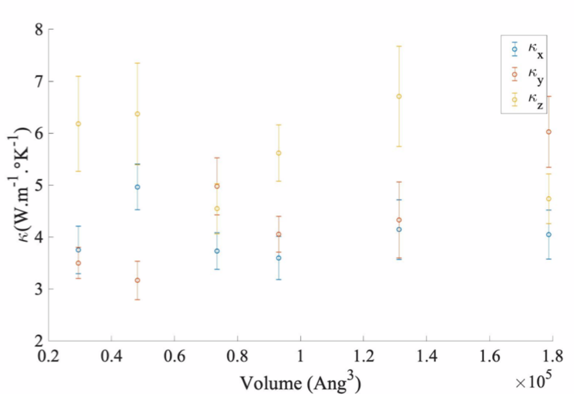

Figure 6.6: Thermal conductivity of $LiAlO_2$ in different axes for different system sizes from MD simulations.

Thermal conductivity with the range of ∼3 to ∼7 $W.m^{-1}K^{-1}$ (at 300 K) for different system size of $LiAlO_2$ obtained using the Green-Kubo method by measuring the thermal fluctuations in equilibrium molecular dynamics simulations where the interatomic forces are modeled using the empirical potentials of Tsuchihira, Oda, and Tanaka (TOT) [103]. The TOT potentials were implemented in LAMMPS using a tabulated form. In these simulations, it takes a long time to average away the long fluctuations in the auto-correlation function and also there is still a large band of uncertainty.

The Green–Kubo method suffers from the difficulty of converging the heat flux vector $J(t)$ and its auto-correlation function. This equilibrium MD approach will always be limited by large uncertainty, even with very long averaging times (for the purpose of narrowing the error bar) — unless we are considering systems in which the phonon lifetimes are short at higher temperatures, or defective crystal. This method also requires bigger computing resources for these calculations.

Due to these limitations, for the next step we considered computing thermal conductivity from non-equilibrium MD simulations. The non-equilibrium method we are using for calculating the thermal conductivity is Muller Plathe method (section 3.7.2), in which one imposes a temperature flux and measures the resulting temperature gradient. MP algorithm exchanges kinetic energy between two particles in different regions of the simulation box which induces a temperature gradient in the system and then base on this gradient the thermal conductivity is calculated. To begin with, we built a long system of $LiAlO_2$ (50x3x3) for Muller Plathe calculations (shown in figure 6.7).

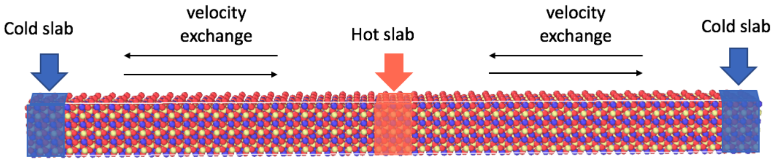

Figure 6.7: Block of $LiAlO_2$ with the size of 50x3x3 for MP calculation of thermal conductivity.

After running MP simulation in ensemble of nve for around 15 ns, the distribution of temperature over the slabs of the system along the long axis (the direction of heat flux, [100]) is represented in the symmetric temperature profile (shown in figures 6.8 and 6.9).

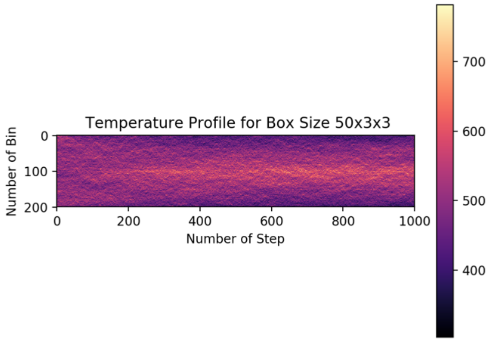

Figure 6.8: Temperature profile of $LiAlO_2$ in MP method.

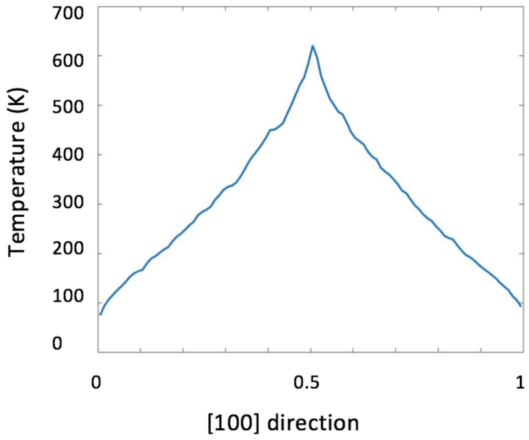

Figure 6.9: Temperature vs position of $LiAlO_2$ block in MP method.

These figures represent the corresponding converged temperature profile through the box along [100] direction. Since the hot and cold layers are separated by the same distance in both directions in a periodic sense, this leads to the symmetric temperature profile. After computing the total kinetic energy transferred by these swaps due to cold-hot slabs, we calculated the thermal conductivity by the ratio of heat flux to the slope of the temperature profile in the cross-sectional area of the simulation box. These calculations predict the [100] thermal conductivity of $LiAlO_2$ at 300 K to be $\sim$7.9 $W.m^{-1}K^{-1}$. Since the temperature gradient is extreme in MP simulations, this explains the deviation of the results from the equilibrium MD simulations.

While these non-equilibrium simulations do not have the statistical sampling problems like the ones in equilibrium simulations, they have a different set of problems including the convergence of systems size (they require orders of magnitude larger systems), ballistic transport, temperature gradient, and the long time taken for the system to reach the steady state.

6.1.2 $LiAlO_2$ with Li Vacancy

In this section, we estimate the effects of Li vacancy on the thermal conductivity of $LiAlO_2$ using MD simulations. The reason for the selection of Li vacancy is that the Li vacancies are expected to be numerous in the system of $LiAlO_2$ as they can be formed by both Li burnup and also by the displacement cascade.

For this purpose, we performed MD simulations using GK method to compute the thermal conductivity of $LiAlO_2$ containing different concentrations of randomly arranged Li vacancies. For defective $LiAlO_2$ with Li vacancies, we should consider: (i) ensuring the balance of charge, (ii) correcting for lattice expansion/contraction, and (iii) correcting the bond stiffness in the vicinity of each vacancy.

For addressing the charge issue in MD simulations using TOT potentials for the $LiAlO_2$ that includes Li vacancies, we compensated for the absent charge of Li^+ by removing the excess electrons uniformly from the charge of the O atoms.

From the point of view of phonons, vacancies may disrupt the crystal in several ways: firstly, they represent a mass defect; secondly, they soften the crystal by removing the bonds of the missing atom, and they also change the strength of the bonding between the remaining atoms which are the neighbours of the vacancy. To understand the underlying stiffness correction, we computed the stiffness matrix for a block of $LiAlO_2$ containing a random Li^+ vacancy, and compared it with the same system without a missing atom.

We performed DFT calculations with empirical potentials, to examine the fidelity of the vacancies in MD model using the stiffness matrix of the atoms surrounding a vacancy. In this approach, we used a 2x2x1 super-cell of perfect $LiAlO_2$ and we calculated the hessian and then in the next step, we removed one Li atom randomly, and again with DFT calculations and the empirical potentials, we computed the hessian after relaxing the structure. For the empirical potentials case, we also compensated the charge of the missing Li. In the next step, we subtracted the equivalent elements of the perfect crystal's stiffness matrix from the stiffness matrix of the defective crystal, to obtain the stiffness change in the vicinity of the vacancy. The stiffness change matrix coming from each calculation is shown in figure 6.10.

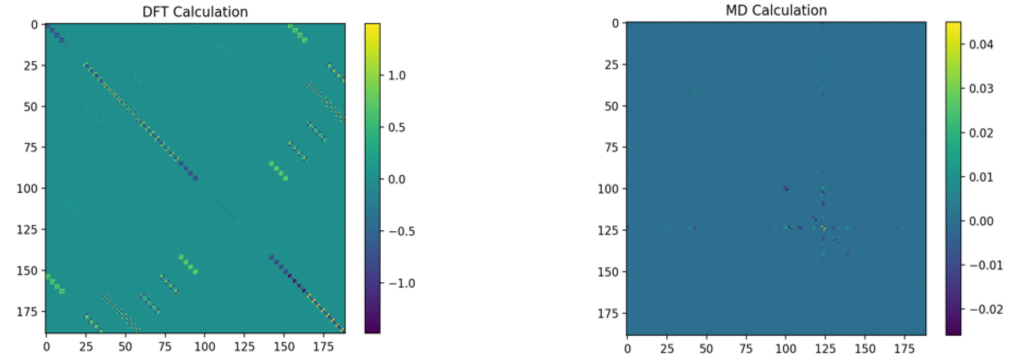

Figure 6.10: Stiffness matrix in the vicinity of the Li vacancy by DFT and MD calculations.

In the next step, we investigated how the extra thermal resistance due to vacancies depends on the vacancy concentration by computing the thermal conductivity of $LiAlO_2$ containing different concentrations of Li vacancies (0.4% and 0.5% Li vacancies). For the comparison, we calculated the thermal resistivity using the GK method for the perfect $LiAlO_2$ as well as the defective $LiAlO_2$ with 0.4 % and 0.5 % vacancy at two different temperatures of 300 K and 1200 K. The thermal resistivity was calculated in 2 directions (x, z) and the result is shown in figure 6.11.

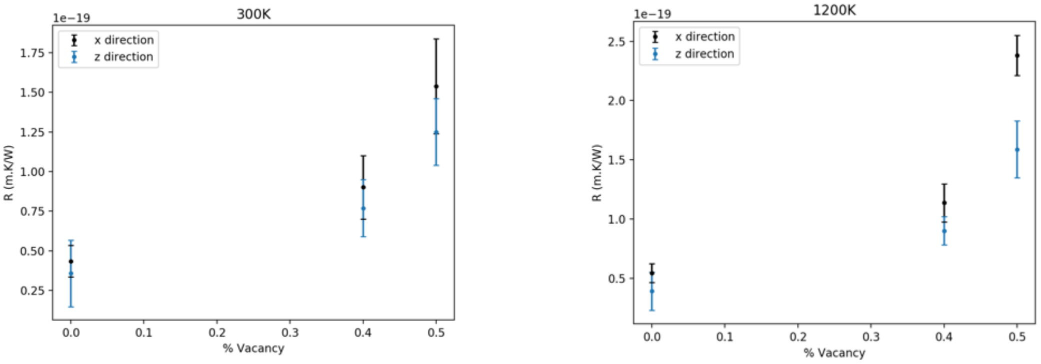

Figure 6.11: Thermal resistivity of pristine and defective $LiAlO_2$ with different concentrations of Li vacancy at 300K (left) and 1200K (right).

The extra thermal resistivity (the reciprocal of the thermal conductivity) has a colligative dependence on the vacancies. Based on the calculations, increasing the concentration of Li causes in a little increase in the resistance in each direction. This is closely related to the phonon scattering in the vacancy of the system.

Surprisingly, the marked increase in resistivity from 0.4% to 0.5% Li vacancies breaks the expected linear trend, both at 300 K and 1200 K, even with the relatively large error bars. The reason could be because the Li vacancies impact the lattice in two ways: (i) they provide centers for phonon scattering due to the local mass/stiffness defect that they cause, and (ii) they can reduce the overall stiffness of the crystal and hence group velocity of the system because of the changes in the charge of the atoms. These results hit at an interesting non-linearity in the thermal resistance with the accumulation of Li vacancies.

6.1.3 $LiAlO_2$ with Interfaces

Grain boundary is another defect which could affect the thermal conductivity of $LiAlO_2$. To investigate this effect, we performed non-equilibrium simulations of systems containing grain boundaries to compute the interfacial thermal conductance. We mainly focused on developing a new general theory to describe the interfacial thermal conductance (ITC) of an interface. ITC is a measure of how efficiently heat carriers flow from one material to another [104, 105]. Typical existing models of phonon scattering at interfaces are the diffuse mismatch model (DMM) [106, 107] and acoustic mismatch model (AMM) [108] that describe the probability that phonons incident at an interface is transmitted through the interface based on the properties of the materials on either side of the interface. These transmission probabilities can then be used in integrals over all the phonon modes to compute the net thermal conductance at an interface. The DMM and AMM assign transmission coefficient regardless of the structure of the interface, and only the bulk property of the two materials on either side of it matters. Generally, DMM model assumes that phonons lose memory of their origin after being scattered by the interface. DMM is only correct at very high temperature where short wavelength phonons are populated and their wavelength is comparable to the surface roughness; on the contrary, AMM assumes phonons as plane wave experiencing specular scatter at the interface (valid at low temperature where only high wavelength phonons are excited).

In our approach, we developed a modified DMM model that also depends on the density of vibrational states at the interface. This acknowledges that the structure and vibrational behavior of the material in the vicinity of an interface is very different from the bulk. This approach accounts for interface localized vibrational modes and the modes which are evanescent across the interface.

Typically, the ITC cannot be measured in equilibrium simulations as at interfaces between dissimilar materials the phonon radiance in each material can be very different, and thus the way that the materials deviate from equilibrium for a given heat flux can be different. Therefore, we computed the ITC via non-equilibrium MP simulations of tilt boundaries in $LiAlO_2$. The system with a pair of tilt boundaries of $LiAlO_2$ is represented in figure 6.12. This system is symmetric around the interface.

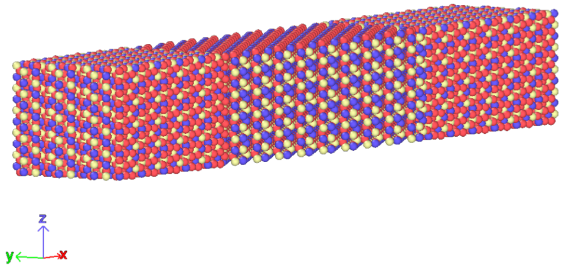

Figure 6.12: 45 degree tilt boundary in $LiAlO_2$.

At the same time, we have performed equilibrium MD simulations on the same block of $LiAlO_2$ containing a pair of tilt interfaces in order to determine the ITC. Like the other equilibrium MD simulations, we used the GK method to compute the thermal conductivity, κ, of the full system including the grain boundaries [109]. Then, by knowing the length L of the compute cell along with the thermal conductivity of the perfect crystal, κ_B, we can infer the thermal conductance, C_I of the interfaces which is defined by:

$$C_I = \frac{2\kappa\kappa_B}{L(\kappa_B - \kappa)} \tag{6.4}$$

or by using Kapitza length (L) [110], we can obtain the estimate for Δ:

$$\Delta = \frac{L}{2}(\frac{\kappa_B}{\kappa} - 1) \tag{6.5}$$

By measuring this temperature step at the interface, the Kapitza length of 6.2 nm was obtained. This length indicates the thickness of thermal resistance that the material at the interface is equivalent to.

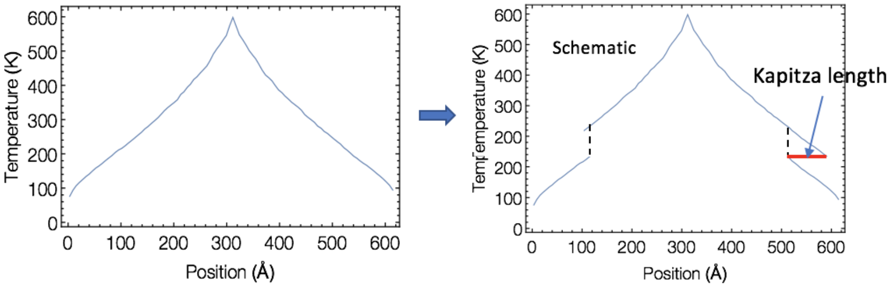

Figure 6.13: Kapitza length at the interface of $LiAlO_2$.

6.1.4 $LiAl_5O_8$

In this section, we focus on calculating the thermal conductivity for $LiAl_5O_8$. $LiAl_5O_8$ is also used as a potential coating material in Li-ion batteries. This system can represent the extreme form of Li vacancies in $LiAlO_2$. The structure of $LiAl_5O_8$ is shown in figure 6.14

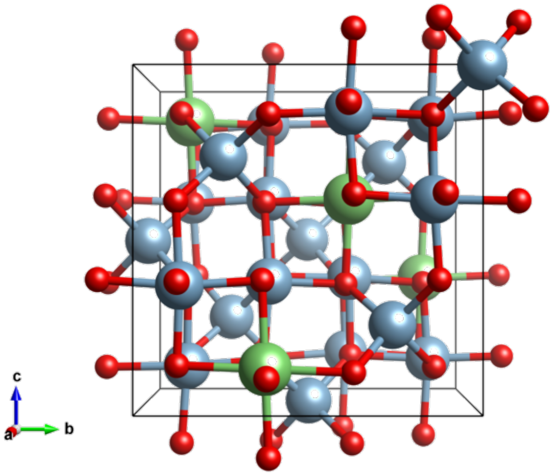

Figure 6.14: LiAl5O8 structure. Red, green and blue atoms belong to Oxygen, Lithium and Aluminum respectively.

For this system, calculating the MD equilibrium thermal conductivity poses some limitations for using the $LiAlO_2$ TOT empirical potentials, since these potentials are not directly transferable to $LiAl_5O_8$. The coulombic interactions between ions in the TOT potentials were modeled using effective charges of +0.7, +1.5, and -1.1 on the Li, Al and

O ions, respectively. The problem is that this ratio of effective charges is not compatible (charge neutral) with the 1:5:8 stoichiometry of $LiAl_5O_8$. The simplest change is to reduce the effective charge of the O to -1.025. However, since we have no physical justification for this, a better and more rigorous approach is to sweep through a range of effective charges that meet the constraint of charge neutrality and search for parameters that best make the system match the experimental lattice constant, and the DFT computed phonon dispersion relation.

To be more systematic, in an attempt we have computed the phonon dispersion for a series of effective charges, changing from -0.9 to -1.5 during which the Li/Al charge ratio was fixed at 1/3 (note that in the $LiAlO_2$ potential, this ratio is 7/15). Since the results had lots of instability generating imaginary vibrational frequencies, and even the crystal was adopting a different crystal symmetry, we concluded that we do not need to modify the $LiAlO_2$ potential for $LiAl_5O_8$ much, and we should focus our search on just tuning the charge initially. Then we ran MD simulations of equilibrium GK for 10 snapshots of $LiAl_5O_8$. We started the simulation on each of these snapshots by 50 ps of nve to lose memory of the prior simulations, and then the simulation was continued for a further 2 ns during which the correlation function was computed. We ran these simulations at 4 different temperatures of 300K, 500K, 800K and 1200K. By increasing the temperature, the average thermal conductivity of $LiAl_5O_8$ over the different axes is decreasing, which is coming from the anharmonic scattering that is inversely proportional to the temperature changes. In other words, as the temperature increases from 300K to 1200K, the ions' vibrations increase (in turn decreasing the mean free path of molecules). So, they obstruct the flow of free electrons, thus reducing the heat conductivity. Figure 6.15 represents the calculated thermal conductivity of $LiAl_5O_8$ in 3 different axes ([100], [010] and [001]) at different temperatures of 300, 500, 800 and 1200 K.

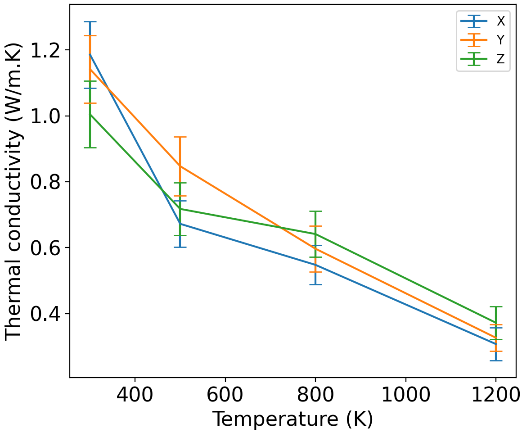

Figure 6.15: Thermal conductivity of $LiAl_5O_8$ at different temperatures.

The calculated thermal conductivities for $LiAl_5O_8$ are much lower than the previously calculated thermal conductivities for $LiAlO_2$. The problem should be related to the transferred TOT potentials due to imbalance of effective charges.

To address this, in another attempt, we used simple Buckingham potential in a core shell model [111] where charges of $LiAl_5O_8$ could be simply modeled. With the new potentials, larger thermal conductivity (10.9 $Wm^{-1}K^{-1}$) was predicted for $LiAl_5O_8$ at 300 K which is more comparable to the $LiAlO_2$ results. These thermal conductivity results are reported in table 6.1.

	[100]	[001]
TOT	1.2 $Wm^{-1}K^{-1}$	1.1 $Wm^{-1}K^{-1}$
Buckingham	10.6 $Wm^{-1}K^{-1}$	25.7 $Wm^{-1}K^{-1}$

Table 6.1: Calculated thermal conductivity for $LiAl_5O_8$ with TOT and Buckingham potential energy.

In summary, this study established atomistic simulation models to highlight the contribution of different scales of defects to thermal properties of a crystalline $LiAlO_2$. We also investigated the uncertainties in these predictions and sources of the error as well as the necessities to modify the empirical potentials when studying the effect of well-defined defects.

Chapter 7

Conclusions

We have been able to draw some important conclusions regarding the structures of defects in materials and link the properties of a material to its local defective structures intimately. In particular, through characterizing the packing behaviours of glass-forming liquids, we elucidated that there is a quantitative correlation between atomic size mismatches and kinetic viscosity behaviour of fragility in super-cooled region. We indicated that size-mismatch can bring more degrees of freedom in the ways that the atoms can pack together so this would affect the fragility behaviour in amorphous liquids. But there is a lot of uncertainty in which the peak positions are changing in PDFs. These peak positions depend on thermal expansion, and atomic distances and they might not be efficient enough to indicate how the structural behaviour of the liquid is changing.

We have furthermore determined the effect of well-defined defects on thermal properties of crystalline structures. Understanding the various types of defects and their contribution to evolution of thermal conductivity under embedded uncertainty estimates. Our results suggested that point defects and grain boundaries can reduce the thermal conductivity of the materials.

Additionally, we developed a simple and efficient model to establish the concepts for identifying outliers in amorphous structures. The model was capable of revealing the local configurations which possess rare structural behaviour. These identified configurations mimic the behaviour of vacancies in crystalline structures and they are in charge of the mechanical response and events that occur while deforming the material. The development of the proposed model will advance the application of amorphous structures in two-fold objective: (i) it provides a better understanding of the variations in packing behaviour (ii) it allows us to connect the types of defects that can be formed with the elemental makeup of the alloy. This combination can provide theoretical guidance for the development of new amorphous structures with predictable mechanical properties.

Bibliography

[1] Zbigniew H Stachurski. On structure and properties of amorphous materials. *Materials*, 4(9):1564–1598, 2011.

[2] Dan Wei, Jie Yang, Min-Qiang Jiang, Lan-Hong Dai, Yun-Jiang Wang, Jeppe C Dyre, Ian Douglass, and Peter Harrowell. Assessing the utility of structure in amorphous materials. *The Journal of chemical physics*, 150(11):114502, 2019.

[3] Walter Bollmann. *Crystal defects and crystalline interfaces*. Springer Science & Business Media, 2012.

[4] E Kröner. The differential geometry of elementary point and line defects in bravais crystals. *International Journal of Theoretical Physics*, 29(11):1219–1237, 1990.

[5] Wai-yim Ching and Paul Rulis. Application to impurities, defects, and surfaces. In *Electronic Structure Methods for Complex Materials*. Oxford University Press.

[6] Meijie Tang, Luciano Colombo, Jing Zhu, and T Diaz De La Rubia. Intrinsic point defects in crystalline silicon: Tight-binding molecular dynamics studiesof self-diffusion, interstitial-vacancy recombination, and formation volumes. *Physical Review B*, 55(21):14279, 1997.

[7] RJ Kurtz, RG Hoagland, and JP Hirth. Effect of extrinsic grain-boundary defects on grain-boundary sliding resistance. *Philosophical Magazine A*, 79(3):665–681, 1999.

[8] Blas Pedro Uberuaga, Louis J Vernon, Enrique Martinez, and Arthur F Voter. The relationship between grain boundary structure, defect mobility and grain boundary sink efficiency. *Scientific reports*, 5(1):1–9, 2015.

[9] Wei-Hua Wang, Chuang Dong, and CH Shek. Bulk metallic glasses. *Materials Science and Engineering: R: Reports*, 44(2-3):45–89, 2004.

[10] John R Scully, A Gebert, and Joe H Payer. Corrosion and related mechanical properties of bulk metallic glasses. *Journal of Materials Research*, 22(2):302–313, 2007.

[11] Morgana Martin Trexler and Naresh N Thadhani. Mechanical properties of bulk metallic glasses. *Progress in Materials Science*, 55(8):759–839, 2010.

[12] HF Li and YF Zheng. Recent advances in bulk metallic glasses for biomedical applications. *Acta biomaterialia*, 36:1–20, 2016.

[13] Dmitri V Louzguine-Luzgin and Jing Jiang. On long-term stability of metallic glasses. *Metals*, 9(10):1076, 2019.

[14] HJ Fecht. Thermodynamic properties of amorphous solids—glass formation and glass transition—(overview). *Materials Transactions, JIM*, 36(7):777–793, 1995.

[15] Ji-Hun Kim, Joon Sik Park, Eun Soo Park, Won Tae Kim, and Do Hyang Kim. Estimation of critical cooling rates for glass formation in bulk metallic glasses through non-isothermal thermal analysis. *Metals and Materials International*, 11(1):1–9, 2005.

[16] Alex Scarani, Alessandro Vona, Danilo Di Genova, Raschid Al-Mukadam, Claudia Romano, and Joachim Deubener. Determination of cooling rates of glasses over four orders of magnitude. *Contributions to Mineralogy and Petrology*, 177(3):1–17, 2022.

[17] AV Sergueeva, N Mara, and AK Mukherjee. Mechanical response of zr-based metallic glass. *Journal of non-crystalline solids*, 317(1-2):169–175, 2003.

[18] Michael P Allen et al. Introduction to molecular dynamics simulation. *Computational soft matter: from synthetic polymers to proteins*, 23(1):1–28, 2004.

[19] Ernst Hairer, Christian Lubich, and Gerhard Wanner. Geometric numerical integration illustrated by the störmer–verlet method. *Acta numerica*, 12:399–450, 2003.

[20] Calvin C Moore. Ergodic theorem, ergodic theory, and statistical mechanics. *Proceedings of the National Academy of Sciences*, 112(7):1907–1911, 2015.

[21] Steve Plimpton. Fast parallel algorithms for short-range molecular dynamics. *Journal of computational physics*, 117(1):1–19, 1995.

[22] Philip M Morse and Herman Feshbach. Methods of theoretical physics. *American Journal of Physics*, 22(6):410–413, 1954.

[23] Murray S Daw, Stephen M Foiles, and Michael I Baskes. The embedded-atom method: a review of theory and applications. *Materials Science Reports*, 9(7-8):251–310, 1993.

[24] Loup Verlet. Computer" experiments" on classical fluids. i. thermodynamical properties of lennard-jones molecules. *Physical review*, 159(1):98, 1967.

[25] Kerson Huang. *Statistical mechanics.* John Wiley & Sons, 2008.

[26] Ken A.. Dill and Sarina Bromberg. *Molecular driving forces: statistical thermodynamics in chemistry and biology.* Garland Science, 2003.

[27] Hermann von Helmholtz, Johann Wilhelm Hittorf, and Johannes Diderik Waals. *Physical Memoirs Selected and Translated from Foreign Sources.* Taylor & Francis, 1888.

[28] Josiah Willard Gibbs. *Elementary principles in statistical mechanics: developed with especial reference to the rational foundations of thermodynamics.* C. Scribner's sons, 1902.

[29] David Sholl and Janice A Steckel. *Density functional theory: a practical introduction.* John Wiley & Sons, 2011.

[30] Georg Kresse and Jürgen Hafner. Ab initio molecular dynamics for liquid metals. *Physical review B*, 47(1):558, 1993.

[31] Zoubin Ghahramani. Unsupervised learning. In *Summer school on machine learning*, pages 72–112. Springer, 2003.

[32] Lior Rokach and Oded Maimon. Clustering methods. In *Data mining and knowledge discovery handbook*, pages 321–352. Springer, 2005.

[33] Zhi-Hua Zhou. A brief introduction to weakly supervised learning. *National science review*, 5(1):44–53, 2018.

[34] Alex Ratner, Paroma Varma, and Braden Hancock. Weak supervision: A new programming paradigm for machine learning—sail blog. *Visited on*, 6(26):2020, 2019.

[35] Alexander Ratner, Stephen H Bach, Henry Ehrenberg, Jason Fries, Sen Wu, and Christopher Ré. Snorkel: Rapid training data creation with weak supervision. In *Proceedings of the VLDB Endowment. International Conference on Very Large Data Bases*, volume 11, page 269. NIH Public Access, 2017.

[36] Merlin C Wittrock. A generative model of mathematics learning. *Journal for Research in Mathematics Education*, pages 181–196, 1974.

[37] Peter Beyerlein. Discriminative model combination. In *1997 IEEE Workshop on Automatic Speech Recognition and Understanding Proceedings*, pages 238–245. IEEE, 1997.

[38] PA Burrough, RA McDonnell, and CD Lloyd. 8.11 nearest neighbours: Thiessen (dirichlet/voroni) polygons. *Principles of Geographical Information Systems*, 2015.

[39] Chris Rycroft. Voro++: A three-dimensional voronoi cell library in c++. Technical report, Lawrence Berkeley National Lab.(LBNL), Berkeley, CA (United States), 2009.

[40] Daniel B Miracle, Eric A Lord, and Srinivasa Ranganathan. Candidate atomic cluster configurations in metallic glass structures. *Materials transactions*, 47(7):1737–1742, 2006.

[41] Linus Pauling. The principles determining the structure of complex ionic crystals. *Journal of the american chemical society*, 51(4):1010–1026, 1929.

[42] James MacQueen et al. Some methods for classification and analysis of multivariate observations. In *Proceedings of the fifth Berkeley symposium on mathematical statistics and probability*, volume 1, pages 281–297. Oakland, CA, USA, 1967.

[43] Richard JD Tilley. *Crystals and crystal structures*. John Wiley & Sons, 2020.

[44] Liang Fu and Charles L Kane. Topological insulators with inversion symmetry. *Physical Review B*, 76(4):045302, 2007.

[45] Xingxing Yue, Akihisa Inoue, Chain-Tsuan Liu, and Cang Fan. The development of structure model in metallic glasses. *Materials Research*, 20:326–338, 2017.

[46] Jean-Pierre Hansen and Ian R McDonald. Theory of simple liquids. *Physics Today*, 41(10):89–90, 1988.

[47] Simon JL Billinge. The rise of the x-ray atomic pair distribution function method: a series of fortunate events. *Philosophical Transactions of the Royal Society A*, 377(2147):20180413, 2019.

[48] Valentin Levashov and MF Thorpe. The shape of the pair distribution function.

[49] Albert P Bartók, Risi Kondor, and Gábor Csányi. On representing chemical environments. *Physical Review B*, 87(18):184115, 2013.

[50] Marcel F Langer, Alex Goeßmann, and Matthias Rupp. Representations of molecules and materials for interpolation of quantum-mechanical simulations via machine learning. *arXiv preprint arXiv:2003.12081*, 2020.

[51] Lauri Himanen, Marc O. J. Jäger, Eiaki V. Morooka, Filippo Federici Canova, Yashasvi S. Ranawat, David Z. Gao, Patrick Rinke, and Adam S. Foster. DScribe: Library of descriptors for machine learning in materials science. *Computer Physics Communications*, 247:106949, 2020.

[52] Paul J Steinhardt, David R Nelson, and Marco Ronchetti. Bond-orientational order in liquids and glasses. *Physical Review B*, 28(2):784, 1983.

[53] Bing-Yang Cao and Zeng-Yuan Guo. Equation of motion of a phonon gas and non-fourier heat conduction. *Journal of Applied Physics*, 102(5):053503, 2007.

[54] Sebastian G Volz and Gang Chen. Molecular-dynamics simulation of thermal conductivity of silicon crystals. *Physical Review B*, 61(4):2651, 2000.

[55] Wei Lv and Asegun Henry. Direct calculation of modal contributions to thermal conductivity via green–kubo modal analysis. *New Journal of Physics*, 18(1):013028, 2016.

[56] Florian Müller-Plathe. A simple nonequilibrium molecular dynamics method for calculating the thermal conductivity. *The Journal of chemical physics*, 106(14):6082–6085, 1997.

[57] Takamichi Terao, Enrico Lussetti, and Florian Müller-Plathe. Nonequilibrium molecular dynamics methods for computing the thermal conductivity: Application to amorphous polymers. *Physical Review E*, 75(5):057701, 2007.

[58] Srikanth Sastry. The relationship between fragility, configurational entropy and the potential energy landscape of glass-forming liquids. *Nature*, 409(6817):164–167, 2001.

[59] Aleksandra Drozd-Rzoska, Sylwester J Rzoska, and Szymon Starzonek. New paradigm for configurational entropy in glass-forming systems. *Scientific Reports*, 12(1):1–9, 2022.

[60] Isabella Gallino, Jan Schroers, and Ralf Busch. Kinetic and thermodynamic studies of the fragility of bulk metallic glass forming liquids. *Journal of Applied Physics*, 108(6):063501, 2010.

[61] David L Sidebottom. Connecting glass-forming fragility to network topology. *Frontiers in Materials*, 6:144, 2019.

[62] Can Yildirim, J-Y Raty, and Mathieu Micoulaut. Revealing the role of molecular rigidity on the fragility evolution of glass-forming liquids. *Nature communications*, 7(1):1–6, 2016.

[63] Mark Wilson and Philip S Salmon. Network topology and the fragility of tetrahedral glass-forming liquids. *Physical review letters*, 103(15):157801, 2009.

[64] Shuai Wei, Zach Evenson, Isabella Gallino, and Ralf Busch. The impact of fragility on the calorimetric glass transition in bulk metallic glasses. *Intermetallics*, 55:138–144, 2014.

[65] Jing Guo, Xiufang Bian, Xuelian Li, and Chunzhi Zhang. Evaluation of liquid fragility for glass-forming alloys based on mixing enthalpy and mismatch entropy. *Intermetallics*, 18(5):933–937, 2010.

[66] Kenneth F Kelton. Kinetic and structural fragility—a correlation between structures and dynamics in metallic liquids and glasses. *Journal of Physics: Condensed Matter*, 29(2):023002, 2016.

[67] Hajime Tanaka. Relationship among glass-forming ability, fragility, and short-range bond ordering of liquids. *Journal of non-crystalline solids*, 351(8-9):678–690, 2005.

[68] L-M Martinez and CA Angell. A thermodynamic connection to the fragility of glass-forming liquids. *Nature*, 410(6829):663–667, 2001.

[69] Dinghai Huang and Gregory B McKenna. New insights into the fragility dilemma in liquids. *The Journal of chemical physics*, 114(13):5621–5630, 2001.

[70] Li-Min Wang, V Velikov, and CA Angell. Direct determination of kinetic fragility indices of glassforming liquids by differential scanning calorimetry: Kinetic versus thermodynamic fragilities. *The Journal of chemical physics*, 117(22):10184–10192, 2002.

[71] KL Ngai and Osamu Yamamuro. Thermodynamic fragility and kinetic fragility in supercooling liquids: A missing link in molecular liquids. *The Journal of Chemical Physics*, 111(23):10403–10406, 1999.

[72] Shuai Wei, Moritz Stolpe, Oliver Gross, Zach Evenson, Isabella Gallino, William Hembree, Jozef Bednarcik, Jamie J Kruzic, and Ralf Busch. Linking structure to fragility in bulk metallic glass-forming liquids. *Applied physics letters*, 106(18):181901, 2015.

[73] Aidan P Thompson, H Metin Aktulga, Richard Berger, Dan S Bolintineanu, W Michael Brown, Paul S Crozier, Pieter J in't Veld, Axel Kohlmeyer, Stan G Moore, Trung Dac Nguyen, et al. Lammps-a flexible simulation tool for particle-based materials modeling at the atomic, meso, and continuum scales. *Computer Physics Communications*, 271:108171, 2022.

[74] David Turnbull and Morrel H Cohen. Free-volume model of the amorphous phase: glass transition. *The Journal of chemical physics*, 34(1):120–125, 1961.

[75] C Austen Angell. Perspective on the glass transition. *Journal of Physics and Chemistry of Solids*, 49(8):863–871, 1988.

[76] J Ding, M Xu, PF Guan, SW Deng, YQ Cheng, and E Ma. Temperature effects on atomic pair distribution functions of melts. *The Journal of chemical physics*, 140(6):064501, 2014.

[77] Jeetain Mittal, William P Krekelberg, Jeffrey R Errington, and Thomas M Truskett. Computing free volume, structural order, and entropy of liquids and glasses. *Reviews in Computational Chemistry*, 25:125–58, 2007.

[78] RE Nettleton and MS Green. Expression in terms of molecular distribution functions for the entropy density in an infinite system. *The Journal of Chemical Physics*, 29(6):1365–1370, 1958.

[79] Michael Widom and Michael Gao. First principles calculation of the entropy of liquid aluminum. *Entropy*, 21(2):131, 2019.

[80] Noel Jakse and Alain Pasturel. Liquid aluminum: Atomic diffusion and viscosity from ab initio molecular dynamics. *Scientific Reports*, 3(1):1–8, 2013.

[81] Christopher A Schuh, Todd C Hufnagel, and Upadrasta Ramamurty. Mechanical behavior of amorphous alloys. *Acta Materialia*, 55(12):4067–4109, 2007.

[82] To Egami, K Maeda, and V Vitek. Structural defects in amorphous solids a computer simulation study. *Philosophical Magazine A*, 41(6):883–901, 1980.

[83] D Srolovitz, K Maeda, V Vitek, and T Egami. Structural defects in amorphous solids statistical analysis of a computer model. *Philosophical Magazine A*, 44(4):847–866, 1981.

[84] Keisuke Ide, Kenji Nomura, Hideo Hosono, and Toshio Kamiya. Electronic defects in amorphous oxide semiconductors: A review. *physica status solidi (a)*, 216(5):1800372, 2019.

[85] Michael Moshe, Ido Levin, Hillel Aharoni, Raz Kupferman, and Eran Sharon. Geometry and mechanics of two-dimensional defects in amorphous materials. *Proceedings of the National Academy of Sciences*, 112(35):10873–10878, 2015.

[86] Liang Tian, Yue Fan, Lin Li, and Normand Mousseau. Identifying flow defects in amorphous alloys using machine learning outlier detection methods. *Scripta Materialia*, 186:185–189, 2020.

[87] Ekin Dogus Cubuk, RJS Ivancic, Samuel S Schoenholz, DJ Strickland, Anindita Basu, ZS Davidson, Julien Fontaine, Jyo Lyn Hor, Y-R Huang, Y Jiang, et al. Structure-property relationships from universal signatures of plasticity in disordered solids. *Science*, 358(6366):1033–1037, 2017.

[88] Volker L Deringer, Noam Bernstein, Albert P Bartók, Matthew J Cliffe, Rachel N Kerber, Lauren E Marbella, Clare P Grey, Stephen R Elliott, and Gábor Csányi. Realistic atomistic structure of amorphous silicon from machine-learning-driven molecular dynamics. *The journal of physical chemistry letters*, 9(11):2879–2885, 2018.

[89] Søren A Meldgaard, Esben L Kolsbjerg, and Bjørk Hammer. Machine learning enhanced global optimization by clustering local environments to enable bundled atomic energies. *The Journal of Chemical Physics*, 149(13):134104, 2018.

[90] Rocco Meli, Andrew Anighoro, Mike J Bodkin, Garrett M Morris, and Philip C Biggin. Learning protein-ligand binding affinity with atomic environment vectors. *Journal of Cheminformatics*, 13(1):1–19, 2021.

[91] Hervé Abdi and Lynne J Williams. Principal component analysis. *Wiley interdisciplinary reviews: computational statistics*, 2(4):433–459, 2010.

[92] Douglas A Reynolds. Gaussian mixture models. *Encyclopedia of biometrics*, 741(659-663), 2009.

[93] Fabian Pedregosa, Gaël Varoquaux, Alexandre Gramfort, Vincent Michel, Bertrand Thirion, Olivier Grisel, Mathieu Blondel, Peter Prettenhofer, Ron Weiss, Vincent Dubourg, et al. Scikit-learn: Machine learning in python. *the Journal of machine Learning research*, 12:2825–2830, 2011.

[94] Steven Walfish. A review of statistical outlier methods. *Pharmaceutical technology*, 30(11):82, 2006.

[95] Oludare Isaac Abiodun, Aman Jantan, Abiodun Esther Omolara, Kemi Victoria Dada, Nachaat AbdElatif Mohamed, and Humaira Arshad. State-of-the-art in artificial neural network applications: A survey. *Heliyon*, 4(11):e00938, 2018.

[96] Sun-Chong Wang. Artificial neural network. In *Interdisciplinary computing in java programming*, pages 81–100. Springer, 2003.

[97] K Kinoshita, JW Sim, and JP Ackerman. Preparation and characterization of lithium aluminate. *Materials Research Bulletin*, 13(5):445–455, 1978.

[98] SHIN-ICHI HIRANO, Takashi Hayashi, and Tomoyuki Kageyama. Synthesis of lialo2 powder by hydrolysis of metal alkoxides. *Journal of the American Ceramic Society*, 70(3):171–174, 1987.

[99] Alain Degiovanni and Yves Jannot. *Thermal properties measurement of materials.* John Wiley & Sons, 2018.

[100] IV Lienhard and H John. *A heat transfer textbook.* phlogiston press, 2005.

[101] Paul Boone, Hasan Babaei, and Christopher E Wilmer. Heat flux for many-body interactions: corrections to lammps. *Journal of chemical theory and computation*, 15(10):5579–5587, 2019.

[102] Donatas Surblys, Hiroki Matsubara, Gota Kikugawa, and Taku Ohara. Methodology and meaning of computing heat flux via atomic stress in systems with constraint dynamics. *Journal of Applied Physics*, 130(21):215104, 2021.

[103] H Tsuchihira, T Oda, and S Tanaka. Derivation of potential model for lialo2 by simple and effective optimization of model parameters. *Journal of nuclear materials*, 395(1-3):112–119, 2009.

[104] Dongliang Zhao, Xin Qian, Xiaokun Gu, Saad Ayub Jajja, and Ronggui Yang. Measurement techniques for thermal conductivity and interfacial thermal conductance of bulk and thin film materials. *Journal of Electronic Packaging*, 138(4):040802, 2016.

[105] DPH Hasselman and Lloyd F Johnson. Effective thermal conductivity of composites with interfacial thermal barrier resistance. *Journal of composite materials*, 21(6):508–515, 1987.

[106] Pramod Reddy, Kenneth Castelino, and Arun Majumdar. Diffuse mismatch model of thermal boundary conductance using exact phonon dispersion. *Applied Physics Letters*, 87(21):211908, 2005.

[107] Haitao Wang, Yibin Xu, Masato Shimono, Yoshihisa Tanaka, and Masayoshi Yamazaki. Computation of interfacial thermal resistance by phonon diffuse mismatch model. *Materials transactions*, 48(9):2349–2352, 2007.

[108] Ravi Prasher. Acoustic mismatch model for thermal contact resistance of van der waals contacts. *Applied Physics Letters*, 94(4):041905, 2009.

[109] A Maiti, GD Mahan, and ST Pantelides. Dynamical simulations of nonequilibrium processes—heat flow and the kapitza resistance across grain boundaries. *Solid state communications*, 102(7):517–521, 1997.

[110] A Khater and J Szeftel. Theory of the kapitza resistance. *Physical Review B*, 35(13):6749, 1987.

[111] Han Liu, Yipeng Li, Zipeng Fu, Kevin Li, and Mathieu Bauchy. Exploring the landscape of buckingham potentials for silica by machine learning: Soft vs hard interatomic forcefields. *The Journal of Chemical Physics*, 152(5):051101, 2020.

[112] Hannes Wagner, Dennis Bedorf, Stefan Kuechemann, Moritz Schwabe, Bo Zhang, Walter Arnold, and Konrad Samwer. Local elastic properties of a metallic glass. *Nature materials*, 10(6):439–442, 2011.

[113] Pierre Lucas. Fragile-to-strong transitions in glass forming liquids. *Journal of Non-Crystalline Solids: X*, 4:100034, 2019.

[114] Peter Lunkenheimer, Felix Humann, Alois Loidl, and Konrad Samwer. Universal correlations between the fragility and interparticle repulsion of glass-forming liquids. *The Journal of Chemical Physics*, 153(12):124507, 2020.